Research Square

Preprints are preliminary reports that have not undergone peer review.
They should not be considered conclusive, used to inform clinical practice,
or referenced by the media as validated information.

Seasonal hydrogeochemical controls on toxic-metal contamination and human health risks in a copper-mining groundwater system

Bhavya Swami
Indian Institute of Technology Roorkee
Manish Kumar
24dr029@iitism.ac.in

Indian Institute of Technology Dhanbad
Emmanuel Daanoba Sunkari
Sir Padampat Singhania University
Rajesh Kumar
Central University of Rajasthan
Anupma Kumari
Patna University
Ramesh Kumar
Tilka Manjhi Bhagalpur University

Research Article

Keywords: Groundwater hydrogeochemistry, toxic metals, copper mining, seasonal variation, saturation indices, positive matrix factorization, human-health risk assessment

Posted Date: November 20th, 2026

DOI: https://doi.org/10.21203/rs.3.rs-11362885/v1

License: This work is licensed under a Creative Commons Attribution 4.0 International License.
Read Full License

Additional Declarations: No competing interests reported.

Seasonal hydrogeochemical controls on toxic-metal contamination and human health risks in a copper-mining groundwater system

Bhavya Swami[1, 2], Manish Kumar[1, 3*], Emmanuel Daanoba Sunkari[4,5,6], Rajesh Kumar[1], Anupma Kumari[7], Ramesh Kumar[8]

[1]Department of Environmental Science, Central University of Rajasthan, Ajmer, India

[2]Department of Hydrology, Indian Institute of Technology, Roorkee, Uttarakhand, India.

[3]Department of Environmental Science and Engineering, Indian Institute of Technology, Dhanbad, Jharkhand, India.

[4]Mining Engineering, Department of Integrated and Advanced Technology, School of Engineering and Sciences, Sir Padampat Singhania University, 313601, Udaipur, Rajasthan, India

[5]Centre of Excellence in Environmental Science and Sustainability, Directorate of Environment and Ecology, Sir Padampat Singhania University, 313601, Udaipur, Rajasthan, India

[6]Department of Chemical Sciences, Faculty of Science, University of Johannesburg, Auckland Park 2006, P.O. Box 524, Johannesburg, South Africa

[7]Environmental Biology Laboratory, Department of Zoology, Patna University, Patna, India.

[8]Department of Botany, P.B.S. College, Banka, Tilka Manjhi Bhagalpur University, Bhagalpur, Bihar, India.

*Corresponding author: 24dr029@iitism.ac.in

Abstract

Groundwater in coal-mining regions experiences combined pressure of mineral weathering, mine drainage, agriculture and industrial effluents, that promotes movement of toxic metals and alter aquifer geochemistry. Yet integrated, source apportioned studies that links seasonal hydrogeochemistry to health risk remain scarce. This study integrates seasonal hydrogeochemical characterisation, positive matrix factorisation (PMF) source apportionment, and probabilistic human health risk assessment to unravel the natural and anthropogenic drivers of groundwater quality degradation. Groundwater in this region evolved seasonally from Ca^{+2}-Mg^{+2}-HCO_3^- to Na^+-HCO_3^- facies due to recharge-induced dilution, silicate weathering and cation exchange. Gibb's plot confirms rock-water interaction as the main control on groundwater quality. PCA (70.8-72.0% cumulative variance) and saturation indices both identified carbonate weathering as the principal geogenic control, with calcite, dolomite and fluorite supersaturation in pre-monsoon. The four-factor PMF model traced Cr^{6+} (~77%) and Cd^{2+} (~61%) to mining-industrial inputs and NO_3^- (~96%) to post-monsoon agricultural leaching. Nearly three-fourth of samples were extremely poor (EWQI up to 537.9), and Hazard Index values (adults: 1.31–44.58; children: 4.12–161.09) exceeded the safe threshold in every sample, with children at greatest risk. This results reveal a significant non-carcinogenic threat to human beings and emphasize the urgent need for sustained remediation and groundwater-management approaches to protect the vulnerable communities in mining-affected drylands, measures that closely conform with SDG 3 goal (Good Health and Well-being) and SDG 6 goal (Clean Water and Sanitation) goals, given the major implications of compromised groundwater on safe drinking-water accessibility.

Keywords: Groundwater hydrogeochemistry; toxic metals; copper mining; seasonal variation; saturation indices; positive matrix factorization; human-health risk assessment

Introduction

Water is a crucial resource that supports human life and also contributes to economic progress and environmental protection. The demand of water has been increased more than seven times since the early 20th century to fulfil the need of growing population, increases more pressure on natural resources and posing a pressing threat to long-term sustainability (Kundzewicz, 2009; Benneyworth et al., 2016; Loaiciga et al., 2024; Hamma et al., 2025; Karandish et al., 2025; Loaiciga et a., 2025). As a result of this, groundwater is declining at faster rates. In India, groundwater levels are declining at a rate of 0.1-0.5 m/year (Jasechko et al.,2024, Barman et al., 2025; Janardhan et al.,2023, Nazari et al., 2025), emphasizing the need to protect these resources to maintain both ecological and socio-economic stability. This challenge is especially more intense in arid and semi-arid regions such as Rajasthan, India where surface water is scarce and monsoon dependent, making groundwater the principal source for agricultural production and domestic water supply (Monir et al., 2024; Pande et al., 2025; Guettaia et al., 2025). In addition to concerns regarding water availability, declining groundwater level also carries severe environmental consequences such as degrading quality and value of this resource (Foster et al., 2018; Hasan et al.,2023; Perez et al., 2024; Rohde et al.,2024). Among the various anthropogenic drivers of groundwater depletion, mining activities have emerged as a particularly significant contributor. Mining activities significantly alters the hydrological regime of the aquifers leading to long term declination in groundwater head, shifts in aquifer parameters, and changes in hydrochemistry (Qiao et al., 2011; Sui et al. 2011; Huang and Chen 2012; Sun et al. 2016; Shi et al., 2017; Zhang et al. 2020, Singh et al.,2023; Karki et al.,2026). These changes, in turn, pose a significant risk to both groundwater quality as well as the local environmental settings (Arkoc et al. 2016; Qu et al. 2018; Dávila-Cisneros et al., 2026). In addition to these, mining and metallurgical processes are the primary human activities responsible for releasing metals into the environment, particularly in developing countries

(Giljum et al., 2025). Most studies worldwide have directly linked heavy metal contamination to mining activities, resulting in high metal contamination in surface water, subsurface water, sediments, soils, and even in plant species (Kan et al., 2021; Adnan et al., 2024; Li et al., 2024; Dai et al., 2025, Prusty et al., 2026). In the Hunan state of China, extraction of metals such as Pb, Zn, Cu, and Ag is ongoing, and the industrial waste produced from these ores has an adverse effect on surface and groundwater quality (Liu et al., 2011), sediments (Sun et al., 2011), soils (Li et al., 2014), and even livestock (Zhang et al., 2018). In the Sungun copper Mining region of Iran, concentration of potential trace elements (iron (Fe) and aluminium (Al)) is also found to exceed safe limits (Nasrabadi et al., 2014). Bech et al. (1997) also reported elevated concentration of arsenic (As) and copper (Cu) in water, soil and plant species near a copper mine in the Andes region of northern Peru, clearly showing the strong influence of metal pollution. Amari et al., 2014; Luo et al., 2020, Narayanan et al., 2025; Isah et al., 2026 have observed lower metal content in pre-monsoon season than post-monsoon indicating dry weather can reduce the movement of heavy metal. Heavy metal contamination becomes a serious environmental and health concern because these metals are highly toxic and do not degrade over prolonged periods (Ali et al., 2019; Piwowarska et al., 2024; Mititelu et al., 2025). It may accumulate inside living organisms and disrupt the ecological balance by entering the human food chain through various transport routes, such as water, soil, and crops. These metals may also cause chronic health issues like neural dysfunction, kidney dysfunction, and even cancer (Bade et al., 2013, Briffa et al., 2020; Laoye et al., 2025;). The above literature suggests the need to investigate mining-related groundwater contamination in region-specific contexts, more pronounced in countries with extensive and long-standing mining histories, such as India.

Economic growth of India has significant contribution from mines, but intensive mining activities impose an adverse effect on the environment particularly regions rich in sulfide ores (Holzheid et al., 2024). Khteri copper mine is one of the prominent mines located in the

northeast region of Rajasthan, India. Here, mining operations have been started since 1967 by the government of India. This region hosts both active as well as abandoned mines associated with huge deposits of sulfide-rich waste. When these wastes dump in the open atmosphere, it comes in contact with air and moisture and produces highly acidic runoff carrying various heavy metals in soluble form also called acid mine drainage (Williams, 1975; Atkins & Pooley, 1982). It also results in increased mobility and concentration of metal content (Fe, Cu, Pb, Cd, Cr and As) that may percolate into sub-surface and cause long-term agricultural and human health risk. This region relies extensively on groundwater for domestic as well as irrigational purposes, thereby increasing its vulnerability to contamination risk. But surprisingly very few studies have been carried out in this region that properly investigate the groundwater chemistry. This insufficient baseline data and comprehensive risk assessments may constraint policymakers and environmental managers from making plans for sustainable groundwater use. Despite the limited number of investigations in this region, the available literature remains sparse and spatially discontinuous. Punia and Siddaiah (2017) has accessed heavy metal concentration and found that most of the samples are above the acceptable limit of WHO, 2011 and BIS, 2012. The calculated hazard quotient is in permissible limit at most of the locations. Punia et al., (2019) has also examined potential trace element concentration in mine tailing and nearby soil and states that acidification of tailing enhances the leachate concentration. Punia et al., 2021 has accessed Uranium and heavy metal content and found high content of Uranium is associated with mineral dissolution due to geogenic and anthropogenic processes. Although previous studies have quantified heavy metal concentrations in the Khetri region, they remain largely descriptive, lacking an integrated, process-based understanding of how geogenic and anthropogenic drivers jointly govern groundwater contamination and how these controls vary seasonally. To address this gap, the present study couples hydrogeochemical process identification (Piper and Gibbs diagrams, saturation indices) with multivariate statistics (PCA)

and positive matrix factorisation (PMF) to resolve contaminant sources across pre- and post-monsoon seasons in the Khetri copper belt. These source signatures are further linked to entropy-weighted water quality (EWQI) and age-differentiated, multi-pathway health risk assessment, establishing a direct source-to-risk framework. By capturing monsoon-driven shifts in hydrochemistry, contamination pathways and exposure risk, this study provides a mechanistic basis for targeted groundwater management and remediation in mining-affected drylands, directly supporting SDG 6 (Clean Water and Sanitation) and SDG 3 (Good Health and Well-being), particularly for vulnerable children.

Study area

The Khetri Copper Mine is established in the Jhunjhunu district of Rajasthan, India, and widely recognised for its long-standing and large-scale copper mining operations. It is located within north-westernmost part of the Aravali foothills. This copper belt spreads over 80 Km from Singhana in Jhujhunu district to Sangwara in Sikar district. Kantli river (Kanti fault) flowing along a northwest-southeast direction divides this region into northern and Southern sectors (Gupta et al., 1998). This region lies at an altitude of approximately 350 meters above mean sea level(msl), corresponding to latitude 28.07°N and longitude 75.094°E. Nowadays, active mining operations are only taking place at these three major sites: Kolihan, Madhan-Kudhan, and Banwas. Out of these mines, Kolihan and Banwas together contain over seventy million tonnes of copper extraction with high metal grades ranging from 1.14% to 1.7%. In contrast, the Madhan-Kudhan mines carry approximately sixty-six million tonnes of ore, with mean copper content around 1.12-1.71%.

Geologically, this region is part of the Delhi Supergroup, which comprises the older psammitic Alwar Group and the younger pelitic Ajabgarh Group of soil (Das Gupta, 1998). Metamorphosed mafic volcanic rocks, banded iron formations, conglomerates, and feldspathic

146 sandstones, such as amphibolites and quartzites, are found in the Alwar group. In contrast, the
147 Ajabgarh Group primarily consists of rocks that are metamorphosed from carbonates,
148 siltstones, and shales, including marbles, phyllites, pelitic rocks, and garnet-chlorite-amphibole
149 schists.

150 This area experiences an arid to semi-arid climate with extreme heat, with a temperature range
151 of 45-47°C. In winter, temperatures range from 0°C to 25°C. The average rainfall of this region
152 ranges from 500-560 mm. Soil type are mostly lithosoils and regisols of hill origin with light
153 textured and reddish brown to greyish-brown in colour, overlain by an aquifer system largely
154 dominated by quartzite, schist, phyllite, gneiss and limestone along with post-Delhi intrusive
155 granites and amphibolites. The average thickness of groundwater aquifers lies between 10-15
156 m, unconfined to semi-confined nature within sub-surface secondary porosity (fractures and
157 joints) of the hard rock formations while the surrounding alluvium aquifers are 15-140 m thick
158 and mainly consists of gravel, silt, sand, clay and kankar having 30-70 m thick saturated zone.

159 Groundwater generally flows from the hills towards the northern and eastern part of the regions
160 following the topographic gradient. The flow over steep hard rock terrain is usually faster than
161 gently sloping alluvial plains. The long-term mining activities and associated sulfide mineral
162 dissolution have raised more concerns over acidic drainage and elevated heavy metal loading
163 in sub-surface water posing potential health risks to the nearby population.

164

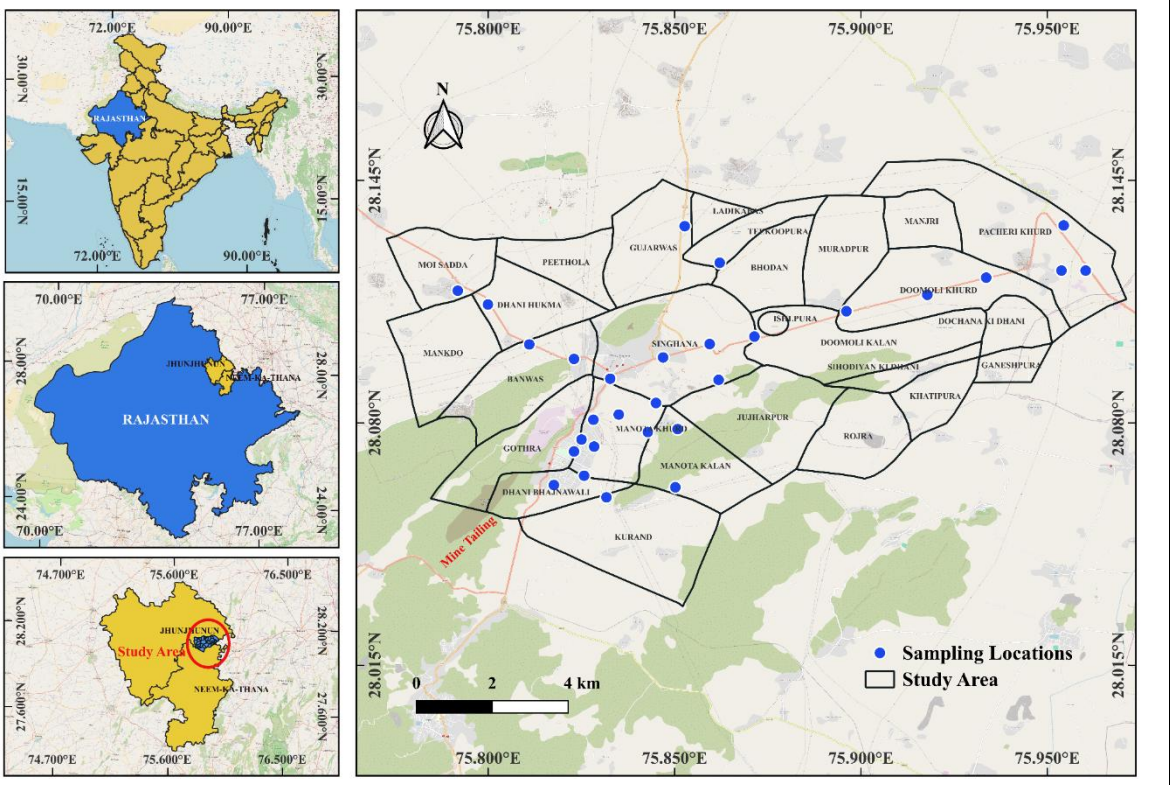

165

166 **Fig. 1** Location of Study area in Jhunjhunu District, Rajasthan, India, showing administrative
167 boundary and sampling well locations and Mine tailing dam.

168 **Materials and methods**

169 **3.1 Sample collection**

170 In total, fifty-nine groundwater samples were collected from Khetri mining region in pre-
171 monsoon season (May 2023) and post-monsoon season (November 2023) using a random
172 sampling approach (Location and source of wells with depth and aquifer material have been
173 given in Supplementary material **Table S1**). Thirty samples have been collected in pre-
174 monsoon season, and twenty-nine samples were collected in post-monsoon season, since a well
175 near the tailing zone of Khetri Mine was found abandoned. The spatial distribution of sampling
176 locations is shown on a Google satellite imagery background using QGIS version 3.44.10 in

Fig. 1. The map clearly indicates that sampling was conducted starting near the Khetri tailings dam and the Khetri copper complex, extending up to 52 km from the mining zone. These samples were collected mainly from public handpumps, private handpumps and borewells dugged inside homes and in fields for personal uses. The main challenge with private handpumps was accessibility and the owner's agreement. Samples were tried to collect in peak water-extraction time to make sure they were indicative of aquifer systems. Handpumps do not seem to be used, are pumped for 15-20 minutes to reduce the risk of contamination and minimize sampling errors. pH, electrical conductivity (EC), and Total dissolved solids (TDS) were measured in the field using portable electrode probe (Oakton probe). Meanwhile, samples were filled in two plastic bottles of 250 ml from every location; out of them, 2-3 drops of HNO_3 were added to one bottle to prevent ion precipitation and used for cation analysis, while the other was left undisturbed for anion analysis because the addition of nitric acid may cause hindrance in concentrations of sulfate and nitrate ions. Finally, these samples were kept in an ice box with ice packs and transported to the laboratory for subsequent chemical analysis.

3.2 Laboratory Analysis

Samples were passed through a filter of 0.45-micron filter in the laboratory before further chemical analysis. Alkalinity was determined by acid-base titration using standardized 0.02 N H_2SO_4 as the titrant. This titrant solution (H_2SO_4) was standardized against a standard sodium carbonate solution (Na_2CO_3) before analysing samples. Water samples are titrated initially to phenolphthalein endpoint (~pH=8.3) using phenolphthalein indicator followed by titration to the total alkalinity endpoint (~pH=4.5) using methyl orange indicator. Bicarbonate concentration (HCO_3^-) were calculated from the amount of titrant used and normality of acid using equation (i);

200 $$HCO_3^- = \frac{V_{(H_2SO_4)} \times N_{(H_2SO_4)} \times 61000}{V_{sample}} \quad (i)$$

201 Here, HCO_3^- measured in mg/L, $V_{(H2SO4)}$ is volume of titrant used and $N_{(H2SO4)}$ is the
202 Normality of titrant and $V_{(sample)}$ is the amount of sample used for titration. Bicarbonate
203 concentration was calculated from the total alkalinity and phenolphthalein alkalinity end
204 point reading and expressed in mg/L. The calculated concentrations were verified through
205 triplet analysis, blank sample reading and regular verification of titrant normality. Total
206 hardness and calcium hardness were measured using EDTA titration. Magnesium hardness
207 was calculated using equation (ii), and Ca^{2+} and Mg^{2+} were measured using equations (iii)
208 and (iv), respectively.

209 $$Magnesium\ Hardness = Total\ Hardness - Calcium\ Hardness \quad (ii)$$

210 $$Ca(mg/L) = Calcium\ Hardness \div 4.12 \quad (iii)$$

211 $$Mg\ (mg/L) = Magnesium\ Hardness \div 2.14 \quad (iv)$$

212 Cl^- ions were measured by argentometric titration with $AgNO_3$. Salinity was calculated for each
213 sample using the measured chloride concentration from equation ((v)

214 $$Salinity\ (PPT) = Cl(mg\ /\ L) \times 0.00180665 \quad (v)$$

215 Fluoride was analysed by the SPAND'S method; nitrate and phosphate were measured by
216 colorimetric methods with HNO3 and ammonium molybdate, respectively; and sulfate was
217 measured by a nephelometric method with barium chloride. For measuring these ions, a
218 minimum accuracy of $R^2 > 0.99$ was required for the calibration curves. Sodium and potassium
219 ions have been analyzed using flame photometer using calibration with standard NaCl and KCl

220 solutions. For further statistical analysis, ion charge balance has been calculated for every
221 sample and found within ± 15 % during both seasons indicating reliability of analytical results
222 (Kumar et.al, 2024), while it shows a shift in Net Charge Balance Index (NCBI) from pre-
223 monsoon value (mean: -8.27) to positive value in the post-monsoon season (mean: +9.17),
224 indicating a transition from baseline anion dominance to recharge-induced cation leaching and
225 mineral dissolution.

226 Trace elements, including Fe, Cu, Cr, Cd, and Pb concentrations were analysed using Flame
227 Atomic Absorption Spectroscopy (Agilent Technologies). Instrument was calibrated prior to
228 analysis using serial dilution of a 1000 mg/L metal stock solution (E-Merck, Germany). To
229 maintain analytical accuracy, a blank sample of de-ionized water was analysed after every 10
230 samples. The recovery rate of metal ranged from 90% to 110% of total metal content with
231 standard deviation of less than 10%.

232 **3.3 Entropy water quality index (EWQI)**

233 EWQI is commonly used to access the potability of groundwater (Alizadeh et al., 2018; Su et
234 al., 2017). Unlike conventional calculations that rely on empirical or subjective weighting, this
235 method assigns parameter weights based on entropy because of the inverse relationship
236 between occurrence probability and entropy. A parameter with lower entropy was considered
237 to carry higher informational precision (Gorgij et al., 2017; Subba Rao et al., 2020). pH, TDS,
238 Alkalinity, Total Hardness, Ca, Mg, Cl, SO4, NO3, F, Fe, Cu, Cd, Pb, Cr have been used for
239 the calculation of EWQI. This approach reduces the bias and subjectivity that often affect
240 traditional conventional methods. The calculation of EWQI consists of three major steps. First,
241 a matrix is formed in which all the 20 parameters are listed along with 30 observational values
242 for each season. Then we require normalization of every parameter using equation (vi):

$$Xij = \frac{(\text{aij} - (\text{aij})\text{min}}{((\text{aij})\text{max} - (\text{aij})\text{min})} \qquad (vi)$$

After this, we get a matrix A that consists of all normalized values of the parameters

$$\text{A} = \begin{matrix} \text{X11} & X12 & X1n \\ X21 & X22 & X2n \\ Xm1 & Xm2 & Xmn \end{matrix} \qquad (vii)$$

Then, we calculated a standardized value P_{ij} which tells the probability of occurrence of any j^{th} parameter in the ith sample,

$$P\text{ij} = \frac{(1 + \text{Xij})}{(\sum(1 + \text{Xij})} \qquad (viii)$$

Claude Shannon (1948) gives this equation to calculate the information entropy (ej) for every physicochemical parameter:

$$ej = \frac{-1}{ln(m)} \sum \text{Pij} \times \ln(\text{Pij}) \qquad (ix)$$

Weightage (w_j) to the parameter was assigned based on its entropy; a lower value of entropy indicates a higher weightage. The calculate weight for each parameter have been given in Supplementary Table S9.

$$wj = \frac{1 - ej}{\sum(1 - ej)} \qquad (x)$$

After this, we have calculated the parameter quality rating scale (qi) for each parameter (except pH):

$$qj = \frac{cj}{sj} \times 100 \qquad (xi)$$

where, Cj = Observed concentration (mg/L) of parameters (j) and Sj= Acceptable concentration (mg/L) of that parameter (j).

Since pH does not have any unit, we cannot use equation (x) for its quality scale rating. For q_{pH} were calculated using (He and Wu 2019):

$$qpH = \frac{pH-7}{SpH-7} \times 100 \qquad (xii)$$

where, pH= Observed pH value for samples, S_{pH} = Acceptable pH (8.5) for the drinking water.

Now, after calculating of weight parameter and quality parameter for each parameter, we can calculate the entropy weighted quality index using the following equation:

$$EWQI = \sum wj \times qj \qquad (xiii)$$

Based on the EWQI values, we can classify the water quality using the ranks assigned to the EWQI of the water. The Rank classification is as follows: EWQI < 25 = Good, 25 < EWQI > 50= Moderate, 50 < EWQI > 100= Poor, 100 < EWQI > 150= Very Poor, EWQI > 150= Extremely poor water quality.

3.4 Source Identification using Multivariate analysis

Principal component analysis (PCA) was used for identifying the correlation among different variables. Variables are internally influenced to each other and is described by their component loading and principal components (PCs). We have checked suitability of dataset using Kaiser-Meyer-Olkin (KMO) test, the result (>0.5) shows this dataset is good for analysis (Krishna et al., 2017). Although, significant p-value (<0.05) got from Bartlett's test of sphericity also indicates meaningful correlation existing among the variables. We have applied PCA for both pre-monsoon and post-monsoon datasets separately and considered only those PCs having

eigenvalue > 1for further investigation (Tanwar et al., 2024). We have interpreted PCA outputs: scree plots, bivariate score plots and loading plots and correlation heatmap of factor loadings, these all were generated using Python 3.13.4. Pearson correlation plots ad Hierarchical Clustered Analysis (HCA) were also analysed for this dataset to support outputs generated by PCA.

3.5 Human health risk assessment

The analysis of human health risk associated with exposure of heavy metals present in groundwater follows a well-established model provided by the Environmental Protection Agency USEPA. It is an analysis explaining how consumption, whether through drinking or exposure, can harm human health. We have calculated non-carcinogenic health risks arises from daily exposure to heavy metals through dermal as well as oral pathways and may include genetic or cellular damage, excluding cancer development. Thus, this research applies the following methods to assess associated health risks.

$$CDI\ (oral) = \frac{(\mathrm{Cw} \times\ \mathrm{DI} \times \mathrm{ABS}\ \times\ \mathrm{EF} \times \mathrm{EP})}{(\mathrm{BW} \times \mathrm{AT})} \qquad (xv)$$

$$CDI\ (dermal) = \frac{\mathrm{C_W} \times\ \mathrm{SA} \times\ \mathrm{Kp} \times ABS\ \times\ \mathrm{ET}\ \times\ \mathrm{EF}\ \times\ \mathrm{EP} \times\ \mathrm{CF}}{\mathrm{BW} \times \mathrm{AT}} \quad (xvi)$$

In the equation (xv) and (xvi), Chronic daily intake (CDI) has been classified as CDI (oral) and CDI (dermal) these nomenclatures are based on the routes of intake. C_w is the actual concentration (mg/L) found as result of our analysis, DI is the daily average intake (L/day), ABS is dermal absorption factor, EF stands for exposure frequency (Day/year); ET stands for total duration of exposure (Hour/event); EP is the exposure period (year), BW tells the total weight of Individuals, SA tells the area (cm^2) get exposed for dermal intake, K_p is the

coefficient called skin permeability coefficient; CF stands for unit conversion factor for each element. The value of variables used for calculation of CDI are listed in Table S5.

3.6 Saturation index calculation

The saturation state of groundwater with respect to the major carbonate, sulfate, fluoride and chloride minerals was assessed using the saturation index (SI), defined as:

$$SI = \log (IAP / K_{SP}) \quad (xvii)$$

Where, IAP denotes the ion activity product of the dissolved species in the mineral dissolution reaction, K_{SP} denotes the equilibrium solubility product of the mineral at the sample temperature (Parkhurst and Appelo, 2013). If SI > 0 indicates super-saturation indicates a tendency to precipitate in the solution, SI < 0 indicates under-saturation indicates tendency to dissolve in the solution and SI = 0 indicates equilibrium between precipitation and dissolution. Samples having saturation index between -0.5 to +0.5 are considered in equilibrium state with mineral phase (Deutsch, 1997). The activity of ion (a_i) was calculated from molal concentration (m_i) and activity coefficient (γ_i) using Davies equations (*xviii)*- (*xx):*

$$a_i = \gamma_i * m_i \quad (xviii)$$

$$\log \gamma_i = -A\, z_i^2 \left[\sqrt{I} / (1 + \sqrt{I}) - 0.3\, I\right] \quad (xix)$$

$$I = \frac{1}{2} \Sigma\, m_i z_i^2 \quad (xx)$$

Here, z_i denotes ionic charge, A denotes temperature-dependent Debye-Hückel constant (0.509 at 25 °C), and I denote an ionic strength. The Davies equation is applicable here because ionic strength in all samples was below 0.17 mol kg^{-1}.

Saturation Index has been calculated using PHREEQC databases that uses thermodynamic constants log K and Reaction enthalpy for solving aqueous speciation using number of iterations. For temperature correction we have used Van't Hoff equation and 25 degree Celcius temperature has been considered for all the calculations. Saturation index have been calculated for calcite, aragonite, dolomite, gypsum, anhydrite, fluorite and halite. The equilibrium partial pressure of CO_2 (pCO_2) was calculated from the activity of dissolved CO_2 and Henry's law constant. After calculation, model was validated with standard equilibrium solutions i.e., water in equilibrium with calcite at atmospheric CO_2 gave SI (calcite) = -0.02, and gypsum-saturated water gave SI (gypsum) = 0.00.

3.7 PMF Source identification and factor profiles

Groundwater source approximation was carried out using positive matrix factorization method (PMF; Paatero and Tapper, 1994) using EPA PMF 5.0 model (Norris et al., 2014). PMF breaks the data matrix into several factor contributions (G) and factor profiles (F) by reducing the uncertainty of weighted object function $Q = \Sigma \Sigma (e_{ij}/s_{ij})^2$, with non-negativity constraints on both G and F. This model uses fourteen different variables: TDS, TH, Na^+, Ca^{2+}, Mg^{2+}, Cl^-, HCO_3^-, NO_3^-, SO_4^{2-}, F^-, Cu^{2+}, Pb^{2+}, Cd^{2+} and Cr^{6+} of samples from both pre-monsoon and post-monsoon season. The uncertainties of objective functions have been calculated as $\sqrt{[(EF \times C)^2 + (0.5 \times MDL)^2]}$, where EF stands for analytical error fraction whereas C is the measured concentrations. An uncertainty of 5/6 × MDL was assigned to all the values below MDL replaced with MDL/2. An extra 20% of modelling uncertainty was applied. All the species had

S/N ratio >3 were retained. TDS and TH (Total Hardness) were set as weak to avoid double counting the constituent ions.

Every solutions having 3-6 factors were tested using 20 random seeds base run, the optimal number of factors was calculated from Q(robust)/Q_exp, where Q_exp = n.m strong-p(n+m_strong) from the scaled-residual distribution (lies within ±3) and from physical interpretability. The stability of solution was accessed using bootstrap resampling (100 runs of $r \geq 0.6$), displacement analysis (DISP; dQmax = 4-25) and FPEAK rotations (-1.0 to +1.0). All the factor contribution was reported with bootstrap percentile interval of 5%-95%.

4 Results & Discussion

4.1 Major Ionic Composition and Hydrogeochemical Characterization

The descriptive statistics for the quality parameters of the collected groundwater samples and their comparison with the BIS (2012) are given in Supplementary Table S2. The pH of groundwater samples varies from near neutral to slightly alkaline (6.49-7.94) in the pre-monsoon season and acidic to alkaline conditions (5.98-7.28) in the post-monsoon season, showing enhanced leaching of oxidized sulfide products (e.g., pyrite oxidation products) during monsoonal recharge (Punia et al., 2019; Chouhan, 2025).

$$4FeS_2 + 15O_2 + 14H_2O \rightarrow 4Fe(OH)_3 + 8SO_4^{2-} + 16H^+$$

The Electrical conductivity (EC) of groundwater samples ranges from 434.00 to 6545.00 µS/cm with a mean and standard deviation (masd) of 2936.10 ± 1627.14 µS/cm in the pre-monsoon season and 950.00 to 9300.00 µS/cm (masd: 4023.63 ± 2026.76 µS/cm) in the post-monsoon season, exceeding the WHO and BIS permissible limit of 1500 µS/cm, indicating substantial groundwater contamination with intensified ion mobilization from acid mine drainage and mineral weathering (Chakraborty & Gupta, 2024). Total Dissolved Solids (TDS)

365 value of groundwater samples also exceeds the BIS acceptable limit of 500 mg/L in both the
366 pre-monsoon season (1465.32 ± 814.44 mg/L) and the post-monsoon season (1839.57 ± 818.44
367 mg/L), also suggesting the effect of anthropogenic inputs like agricultural runoff and mining
368 activities (Liu et al., 2024). In samples of pre-monsoon season, a stable near equilibrium ionic
369 composition is found in samples ($R^2 = 0.99$) whereas, in post-monsoon samples this
370 equilibrium gets disturbed due to introduction of fresh rainwater, mobile monovalent ions and
371 un-ionized solutes, lowers the conversion slope ($R^2 = 0.68$) of EC-TDS relationship shown in
372 fig (Supplementary Fig 1).

373 Significant variation in the hydro-chemical behaviour of major cations was observed between
374 the pre- and post-monsoon seasons. During the pre-monsoon season, sodium (Na^+)
375 concentrations ranged from 167.20 to 898.40 mg/L (masd 423.93 ± 186.73 mg/L), indicating
376 its dominance among monovalent cations and suggesting contribution from silicate weathering
377 and possible anthropogenic inputs (Panwar et al., 2025). and in the post-monsoon season 100-
378 779 mg/L (masd: 410.51 ± 199.65 mg/L), reflecting dilution due to recharge but the persistence
379 of geogenic sources. Calcium (Ca^{2+}) varied from 105 to 819 mg/L (masd: 464.59 ± 189.29
380 mg/L), reflecting a strong influence from carbonate mineral dissolution (Kumar et al., 2023)
381 and 33.64 to 370.06 mg/L (masd: 164.19 ± 103.46 mg/L), implying dilution by rainwater
382 recharge and a reduced residence time for water-rock interaction. Magnesium (Mg^{2+}) range
383 from 115 to 1325 mg/L (masd 546.20 ± 330.34 mg/L) and 21.15 to 417.16 mg/L (masd: 202.54
384 ± 121.16 mg/L), indicating a decreased contribution from dolomite dissolution and silicate
385 weathering during the post-monsoon season (Anjali et al., 2025). Potassium (K^+) ranging from
386 3.09 to 18.40 mg/L (masd: 8.79 ± 3.58 mg/L) and 0.20-15.30 mg/L (masd: 7.09 ± 3.53 mg/L),
387 typically reflecting its low mobility and adsorption onto clay minerals. Among the anions,
388 fluoride (F^-) varied from 3.56 to 20.00 mg/L (masd: 9.93 ± 4.06 mg/L), indicating geogenic
389 contribution from fluoride-bearing minerals intensified by evaporation (Das et al., 2017).

Chloride (Cl^-) ranged from 10.00 to 1429.56 mg/L (masd: 452.40 ± 332.98 mg/L), reflecting inputs from saline groundwater sources and possible anthropogenic contamination. (America et al., 2020). Nitrate (NO_3^-) range from 18.00 to 306.00 mg/L (masd: 161.01 ± 89.04 mg/L), indicating a significant influence from agricultural runoff and sewage infiltration (Zhang et al., 2024; Jia et al., 2025). In addition, the use of ammonium nitrate-based explosives (ANFO) for blasting is also responsible for elevated nitrate concentrations (Fida et al., 2025). Sulfate (SO_4^{2-}) ranged from 272.00 to 3088.00 mg/L (masd: 972.81 ± 726.77 mg/L), indicates rock weathering and potential industrial or agricultural inputs. (Srinivasamoorthy et al., 2008; Wang et al., 2019). Phosphate (PO_4^{3-}) ranged from 0.10 to 1.20 mg/L (masd: 0.48 ± 0.33 mg/L), likely controlled by fertilizer application and domestic wastes (Wang et al., 2019). Carbonate (CO_3^{2-}) varied from 10.00 to 60.00 mg/L (masd: 25.17 ± 12.31 mg/L), while bicarbonate (HCO_3^-) ranged from 919.84 to 4400.00 mg/L (masd: 2209.65 ± 990.39 mg/L), confirming dominant carbonate buffering and interaction with host lithology during the pre-monsoon season (Kumar et al., 2017). The overall dominance pattern of major cations and anions was $Mg^{2+} > Ca^{2+} > Na^+ > K^+$ during pre-monsoon season and $Na^+ > Mg^{2+} > Ca^{2+} > K^+$ in post-monsoon season. The relative increase in sodium contribution during the post-monsoon season reflects the enhanced leaching of sodium-bearing minerals and the mobilization of exchangeable sodium from the soil after rainfall infiltration (Khan et al., 2025). While for anions the trend was $HCO_3^- > SO_4^{2-} > Cl^- > NO_3^- > F^- > CO_3^{2-} > PO_4^{3-}$ across both periods.

The hydrogeochemical processes are characterized using graphical representation of Piper plot (Piper, 1944) and Gibb's plot (Gibbs, 1970). Piper plot (Fig. 2) clearly shows a seasonal shift in groundwater facies from heterogeneous mixed-type composition in the pre-monsoon season to a homogenous Na^+-HCO_3^- dominant facies in the post-monsoon season. In pre-monsoon season, samples are mostly Ca^{2+}-Mg^{2+}-HCO_3^-, Ca^{2+}-Mg^{2+}-Cl^--SO_4^{2-}, and Na^+-Cl^--SO_4^{2-} type reflecting mixed geogenic control of carbonate dissolution, silicate weathering and minor

evapourite/ anthropogenic inputs under low water-table condition. In post-monsoon seasons, most of the samples are of Na^+-HCO_3^- type, indicating homogenization due to enhanced monsoonal recharge, cation exchange and silicate weathering. This shift attributes to base-exchange reactions (Ca^{2+}/Mg^{2+} exchanged for clay-adsorbed Na^+) and feldspar weathering, that releases Na^+ and HCO_3^- . Prolonged rock-water interaction during monsoonal infiltration accelerates this weathering pathway, establishing Na^+-HCO_3^- as the dominant post-monsoon hydrochemical facies.

$2NaAlSi_3O_8$ (Sodium Feldspar) + $2H_2CO_3$ + $9H_2O$ $\rightarrow 2Na^+ + 2HCO_3^- + 4H_4SiO_4 +$ $Al_2Si_2O_5(OH)_4$ (Albite Weathering)

This seasonal shift is further explained using bivariate scatter plots (Fig. 3), which quantitatively validate the geochemical processes. The Ca^{2+} + Mg^{2+} versus total cations plot (Fig. 3a) shows pre-monsoon samples clustering near 1:1 isohaline and post-monsoon samples clustering near 1:2 isohaline, indicating stronger Ca^{2+} + Mg^{2+} dominance, which shifts to Na^+ +K^+ in post-monsoon samples, supporting the trend observed in piper plot. The Ca^{2+} versus Mg^{2+} scattered plot (Fig. 3b) shows pre-monsoon samples are above 1:1 line that indicate Ca enrichment from calcite and dolomite dissolution and in post-monsoon, these samples are nearly clustered towards origin with lower Ca and Mg reflecting dilution and cation exchange. Ca^{2+} + Mg^{2+} versus SO_4^{2-}+ HCO_3^- plot (Fig. 3c) indicates the pre-monsoon samples are closer to 1: 1 line supports carbonate weathering in pre-monsoon while the post-monsoon samples are shifted more towards silicate weathering suggests the feldspar hydrolysis process is dominant. Similarly, the chloro-alkaline indices (CAI-1 vs CAI-II) transition (Fig. 3d) from negative values in the pre-monsoon period, indicative of cation exchange, toward the reverse ion-exchange boundary in post-monsoon samples, directly supporting the base-exchange mechanism proposed to explain the Na^+-HCO_3^- convergence. The Na^+ versus Cl^- scatter plot

(Fig. 4a) shows pre-monsoon samples plotting above the halite dissolution line within the silicate weathering/ion exchange domain, confirming that the mixed Na^{+}- Cl^{-}-SO_4^{2-} facies seen in the pre-monsoon originates from silicate weathering and ion exchange rather than evaporite dissolution, while the SO_4^{2-} versus Ca^{2+} plot (Fig. 4b) shows most samples falling below the gypsum dissolution line, ruling out evaporite dissolution as the primary sulfate source and instead pointing to carbonate weathering as the dominant control on excess calcium in pre-monsoon groundwater.

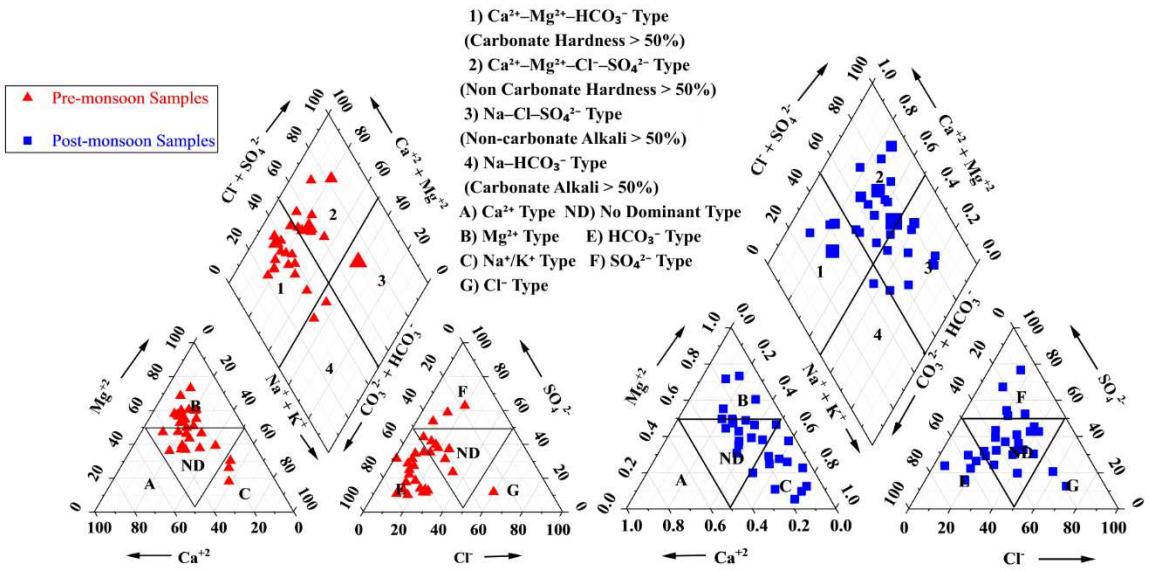

Fig. 2 Piper plot showing the hydrogeochemical nature of groundwater samples for both seasons.

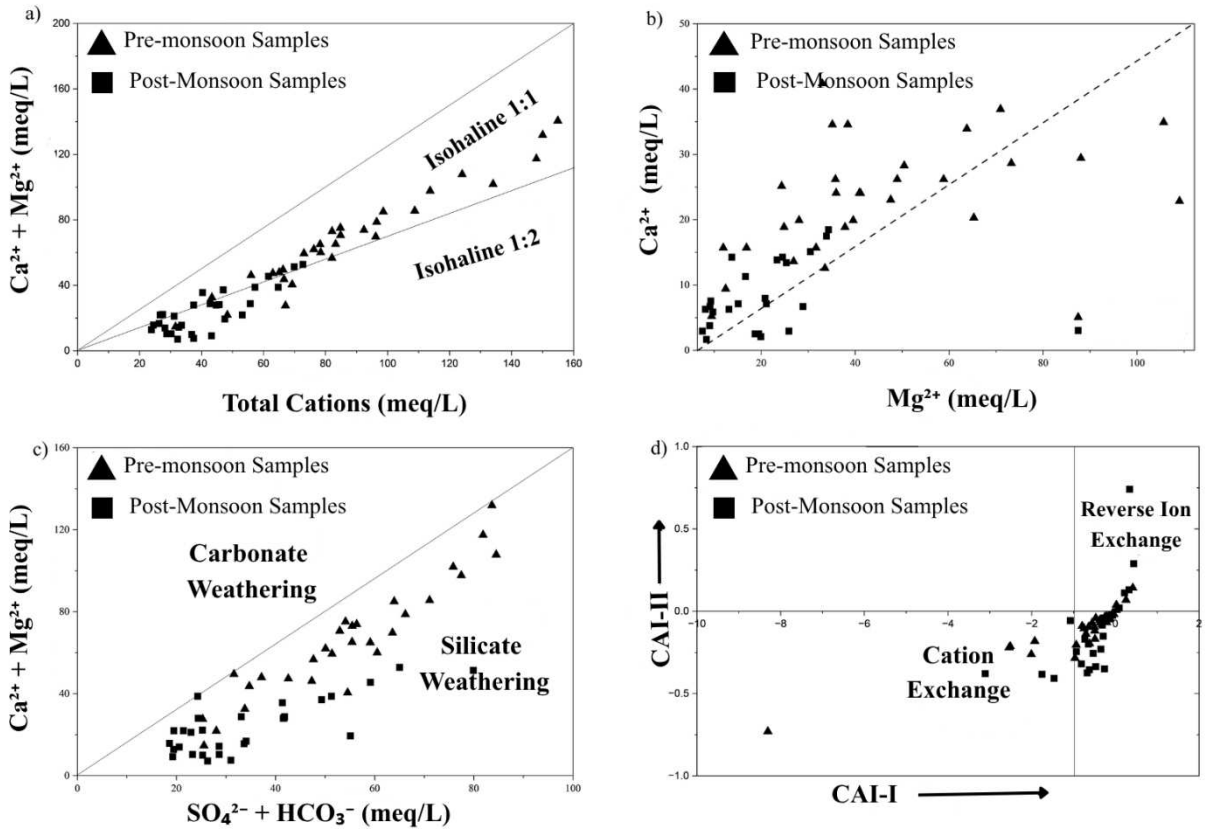

449

450 **Fig. 3** Specific ion relationship Plots between a) $Ca^{+2} + Mg^{+2}$ versus Total cations shows sample
451 falling in Isohaline 1:1 and Isohaline 1:2 zone b) Ca^{+2} versus Mg^{+2} plot c) $Ca^{+2} + Mg^{+2}$ versus
452 $SO_4 + HCO_3^-$ plot d) CAI-I versus CAI-II plot showing processes like cation exchange and
453 reverse ion exchange.

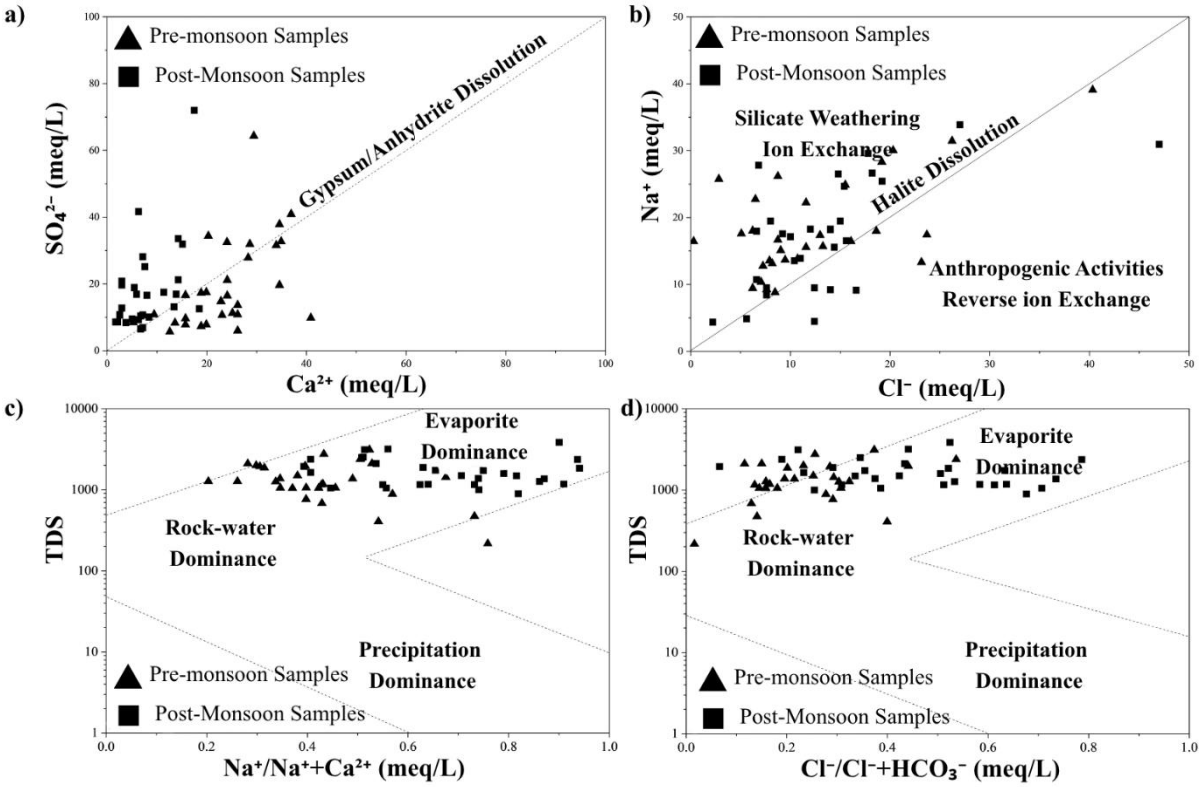

Fig. 4 a) SO_4^{2-} versus Ca^{2+}; b) Na^+ versus Cl^- c) Gibbs Plot (TDS vs Cations) d) Gibbs Plot (TDS vs Anion) showing the hydrogeochemical processes involved.

In addition to this, Gibb's plot (Fig. 4c & 4d) illustrates rock-water interactions as the dominant control on groundwater chemistry, with most of the pre- and post-monsoon samples falling in rock-water dominance across both diagrams. Some of the post-monsoon samples trends towards the evaporation dominance field, with higher ion ratios and total dissolved solids exceeding 3000 mg/L, supporting strong evapo-transpiration in semi-arid zones of Rajasthan. (Wang et al., 2024a, 2024b) In the copper-bearing Khetri-Singhana belt, the rock-water signature mainly reflects weathering of silicate and sulfide-bearing host rocks rather than carbonate/limestone dissolution. Mining and smelting processes may further enhance the ion concentration through exposed ore and tailings, promoting a secondary anthropogenic influence on the natural weathering and evaporative concentration signals.

4.2 Saturation Indices of Minerals

The Saturation Index reflects the equilibrium state between the water phase and mineral phase of solution. We have employed Geochemical modeling software (PHREEQC version 3.8.6) for the calculation of mineral saturation levels involved in groundwater interactions. Overall statistics of mineral saturation indices and their seasonal distribution are given in the Supplementary Table S3. All the samples in pre-monsoon season were found supersaturated with respect to calcite (SI 0.60 to 1.72; median 1.22), aragonite ((0.45 to 1.58; median 1.08) and dolomite (1.20 to 3.88; median 2.84). This tendency reflects high carbonate content in the sample (median 2464 mg L^{-1}) and near-neutral pH (6.5-7.5) before recharge that implies carbonate minerals could precipitate in the aquifer matrix during pre-monsoon season. In the post-monsoon season, the carbonate structuration suddenly drops to calcite from −0.71 to 0.67 (median −0.09), with out of 29 samples 25 samples are in equilibrium range. Dolomite remained supersaturated, but only 13 samples had crossed SI=0.5. This seasonal shift from carbonate supersaturation to equilibrium or near equilibrium caused due to lower pH value (median 6.8 shifts to 6.8) and decrease in bicarbonate ion concentration (median 2464 shifts to 820 mg L^{-1}). Together, it indicates that aquifer alkalinity was consumed by recharge from rainfall during monsoon. Dilution caused due to rainfall play major role in this reduction. Along with this, the high sulphate concentration (313–3457 mg L^{-1}) that comes from oxidation of sulfide minerals is neutralized by carbonate minerals:

$$CaCO_3 + H_2SO_4 \rightarrow Ca^{2+} + SO_4^{2-} + H_2O + CO_2$$

The calculated log pCO_2 in the pre-monsoon season ranged from -1.97 to -0.17 atm (median 0.95) and in post-monsoon season it ranges from -1.55 to 0.14 atm (median -0.91 atm). In both the seasons the values go two to three times beyond the atmospheric level ($10^{-3.4}$ atm) cause increment of soil-zone CO_2 level. pCO_2 had high negative correlation with pH level in both seasons (Spearman ρ = -0.81 and -0.87, $p < 0.001$). The increased pCO_2 indicates a source of

carbon-dioxide addition to soil respiration that is consistent with CO_2 released when carbonates neutralize acidity. All the samples of both seasons were undersaturated with respect to gypsum and anhydrite in pre-monsoon (SI= -1.27 to -0.13; median -0.64) and in post-monsoon (SI= -1.75 to -0.16; median -0.93). The highest sulfate concentration was found in sample 14 of post-monsoon season (3457 mg/L) was also undersaturated (SI=-0.16). Gypsum SI increased systematically with SO_4^{2-} that shows sulfate concentration are mainly controlled by supply rather than mineral solubility ($\rho = 0.95$ pre-monsoon and 0.77 post-monsoon at $p < 0.001$). It reflects that gypsum precipitation therefore does not limit dissolved sulfate and continued increasing SO_4^{2-} reflects continuous input through recharge.

In the pre-monsoon seasons, 27 samples out of 30 are supersaturated with respect to fluorite (SI 0.19 to 1.54; median 0.98), but in post-monsoon period, 21 samples out of 29 were close to the equilibrium (−1.10 to 0.80; median 0.08). Due to supersaturation, the fluoride concentration reaches from 4 mg/L -20 mg/L indicates that fluoride concentrations are near the solubility limit set by Ca^{2+} activity. In the post-monsoon season, due to dilution the fluoride concentration decreases to 2-10 mg/L that brought back water to equilibrium. Since Fluorite limits the fluoride concentration where Ca^{+2} was abundant, the persistently high fluoride points to additional F^- release through ion exchange or dissolution of fluoride-bearing minerals, such as micas and amphiboles, in the host rocks. Halite was strongly undersaturated in both seasons (median SI −5.61 and −5.53). Na^+ and Cl^- are therefore not controlled by halite solubility, and their variation reflects evaporative concentration and mixing rather than mineral equilibrium. Figure 5 (a) accounts for the saturation indices distribution for different mineral solution.

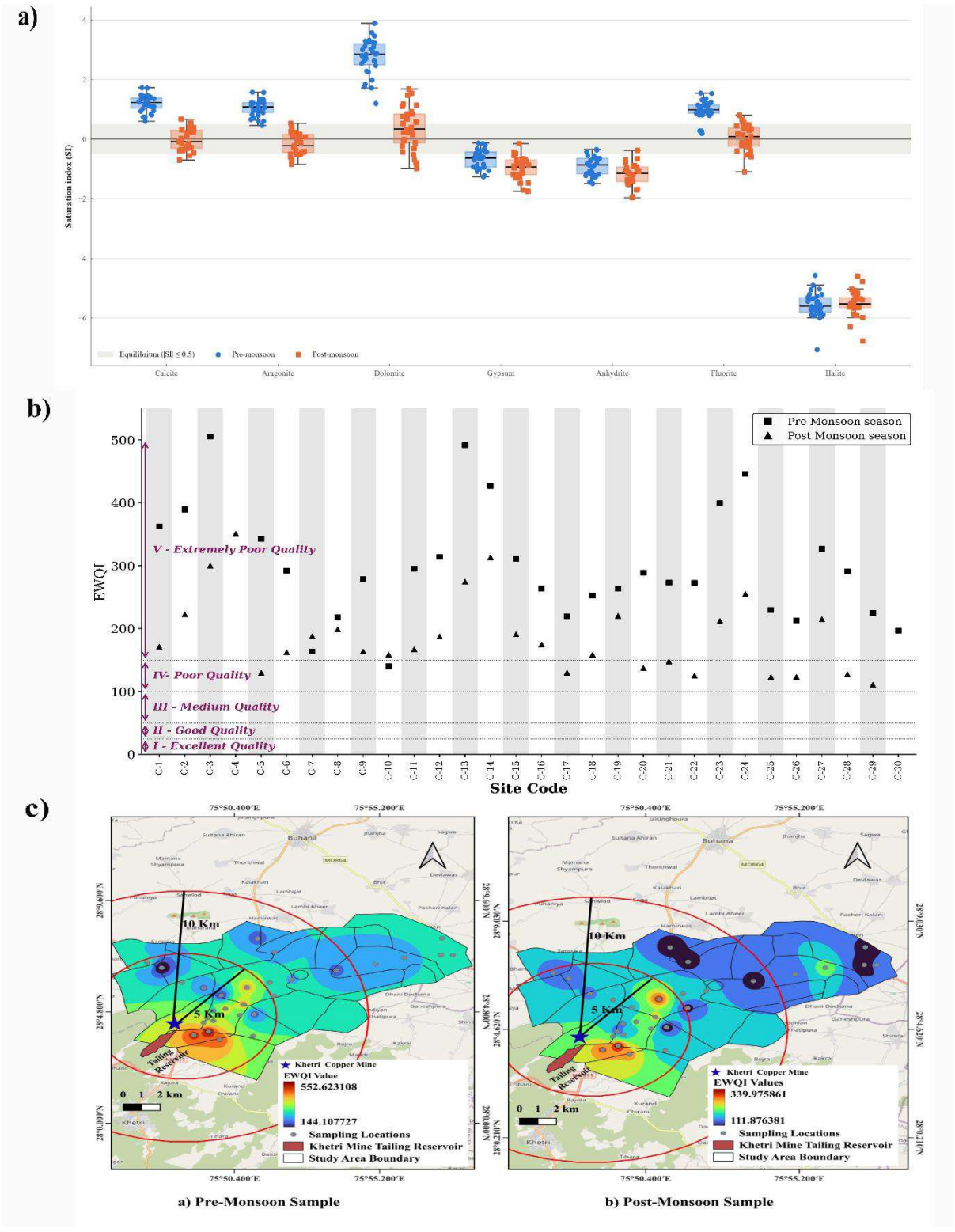

Fig. 5 a) Saturation Indices of minerals: Calcite, dolomite, and aragonite are plotted across different sampling locations of the pre-monsoon and post-monsoon seasons. **b)** Entropy-based

assessment of water quality indicators. **c)** Spatial plot showing the distribution of EWQI at 5 km and 10 km radius across study area region.

The Entropy Weighted Water Quality Index (EWQI) was used for the evaluation of combined effect of water quality parameters and to identify the contamination hotspots linked to subsurface geological formations. Twelve physio-chemical parameters pH, TDS, TH, Na^{+}, Ca^{2+}, K^{+}, Mg^{2+}, F^{-}, Cl^{-}, HCO_3^{-}, SO_4^{2-}, and NO_3^{-} were used for this analysis, following the entropy-based methodology proposed by Dashora et al., (2022). Supplementary Table S9 includes the EWQI values and water quality classes for the pre- and post-monsoon samples. The spatial distribution of EWQI and seasonal changes are plotted in Fig. 5 b and 5c.

The EWQI classification shows the seasonal variation in groundwater quality across the 30 sampling sites for pre- and post-monsoon seasons. The calculated values EWQI values are also given in Supplementary Table S9. During the pre-monsoon season, 90% of samples fall into the Extremely Poor category with EWQI greater than 200, only 3.33% fall under medium category, and the remaining 6.67% fall under Poor quality, indicating severe and widespread contamination across the study area. The post-monsoon samples exhibit a substantial improvement with medium quality sample numbers increasing to 30% whereas, Poor quality accounts 36.67%, and Extremely Poor samples reaches to 33.33% of the total samples. The mean EWQI reduced from approximately 308.74 in pre-monsoon to approximately 187.67 in post-monsoon this significant reduction of approximately 39% states that monsoonal recharge comes in action to dilute contaminant loads without eliminating them.

The spatial distribution of high EWQI values aligns closely with the sub-surface lithology of the Khetri Copper Belt. Sample Nos. 3, 4, and 13 recorded the highest EWQI values in both seasons (566.99, 505.23, and 491.76 in pre-monsoon respectively), lie within the core mineralized zone dominated by garnet-chlorite schist and banded amphibole quartzite, the

principal ore-hosting formations of the belt. The metasedimentary terrains are highly folded and fractured due to their proterozoic tectonic evolution forming secondary voids and interconnected fault networks that enable fast infiltration of sulfide oxidation product and heavy metals from mine waste and tailing or overburden dumps. These structural settings are similar to fractured hard-rock aquifers where, weathering and structural discontinuities are controlling groundwater flow and contamination transport instead of primary voids (Sarkar et al., 1980). Whereas, locations in the close proximity with localized limestone bands of Ajabgarh group composed of calcareous and phyllite minerals (sample 10 and 29) having comparatively lower EWQI values due to lower solubility of carbonate minerals in limestone and its buffering capacity against acid mine drainage reduced the mobility of dissolved contaminant in these zones (Chen et al., 2025). The continued elevated level of EWQI in both seasons irrespective of post-monsoon dilution indicates that recharge may also facilitate contamination leaching from weathered schist and quartzite minerals and exposed mine dumping. At sampling location 7, trend looks reversed (163.72 in pre-monsoon rises to 187.91 in post-monsoon) after getting diluted with monsoonal recharge indicates leaching is more dominant over simple dilution in fractured controlled region near to mine periphery. Overall, the interaction between fractured schist-quartzite formations is responsible for enhanced contamination transport and localised limestone or gneissic zones are reducing, which also explains the spatial heterogeneity observed in the spatial EWQI map.

4.4 Heavy metal content and their associated Health risks

A total of five heavy metals (Fe, Cu, Cd, Pb, and Cr) were analysed in the groundwater samples of pre- and post-monsoon seasons. Their concentrations were found more in the pre-monsoon than the post-monsoon season, indicating dilution effect from the monsoonal recharge. Iron (Fe) recorded the highest values ranging between 1.12 to 8.50 mg/l (masd 2.75 ± 1.84 mg/l)

and 0.47 to 3.51 mg/l (masd 1.349 ± 0.81 mg/l), Cd ranges from 0.004 to 0.03 mg/l (masd 0.025 ± 0.042 mg/L) and 0.005 to 0.018 (masd 0.01 ± 0.03), Pb ranges from 0.03 to 0.27 mg/L (masd 0.10 ± 0.06), Cr ranges from 0.10 and 2.70 mg/l (masd 1.08 ± 0.47 mg/L) and from BDL to 2 mg/L (masd 0.61 ± 0.49 mg/L), Cu ranges from 0.08 to 1.21 mg/l (masd 0.24 ±mg/l) and 0.05 to 0.78 mg/L (masd 0.14 ± 0.15 mg/L) in the pre- and post-monsoon respectively. These all-heavy metals surpass the permissible limit (Fe: 0.3mg/L; Cd: 0.003 mg/L; Pb: 0.01 mg/L; Cr:0.05 mg/L; Cu: 0.05 mg/L) suggested by WHO, 2011 and BIS, 2012 in both the seasons (Permissible limits. Statistical summary of heavy metal concentration has been provided in supplementary Table S4.

A general decline in the heavy metal concentration was observed in the post-monsoon season in comparison with pre-monsoon season indicating the dilution from monsoon recharge. Persistent elevation in concentration of heavy metals across both the seasons indicating a continuous risk. Similar trends of heavy metals have been seen across the world, Siame et al., (2024) also found high concentration of Pb (0.131 mg/L) in groundwater samples due to mining contributions near Kabwe Mine, Zambia. Ikpi et al., (2024) has also reported Pb (0.02-1.28 mg/l) and Cd (0.02-0.81 mg/L) frequently exceeding WHO limits near the Akamkpa quarry district, Nigeria. Whereas Zouhri et al., (2025) observed lower Cd (0.00002-0.00053 mg/l) and Pb (0.00008-0.00358 mg/l) near Karstic chalk aquifers of France indicating less anthropogenic disturbance in that area.

In this study, the persistently high concentration of Cd and Pb in this study comes from anthropogenic sources such as mining induced fractures, overburden rocks and leaching from mine dumps rather than purely geogenic origins, like the pattern reported by Singh et al. (2018) in East Singhbhum, Jharkhand, India. Elevated Fe and Cr concentration indicates the dissolution of iron and chromium bearing minerals of the lithological formations and get

589 compounded due to mining related activities. Overall, presence of these heavy metals is
590 governed by both natural geochemical processes as well as mining activities. The percentage
591 heavy metal content for all the heavy metals has been shown in Fig. 6.

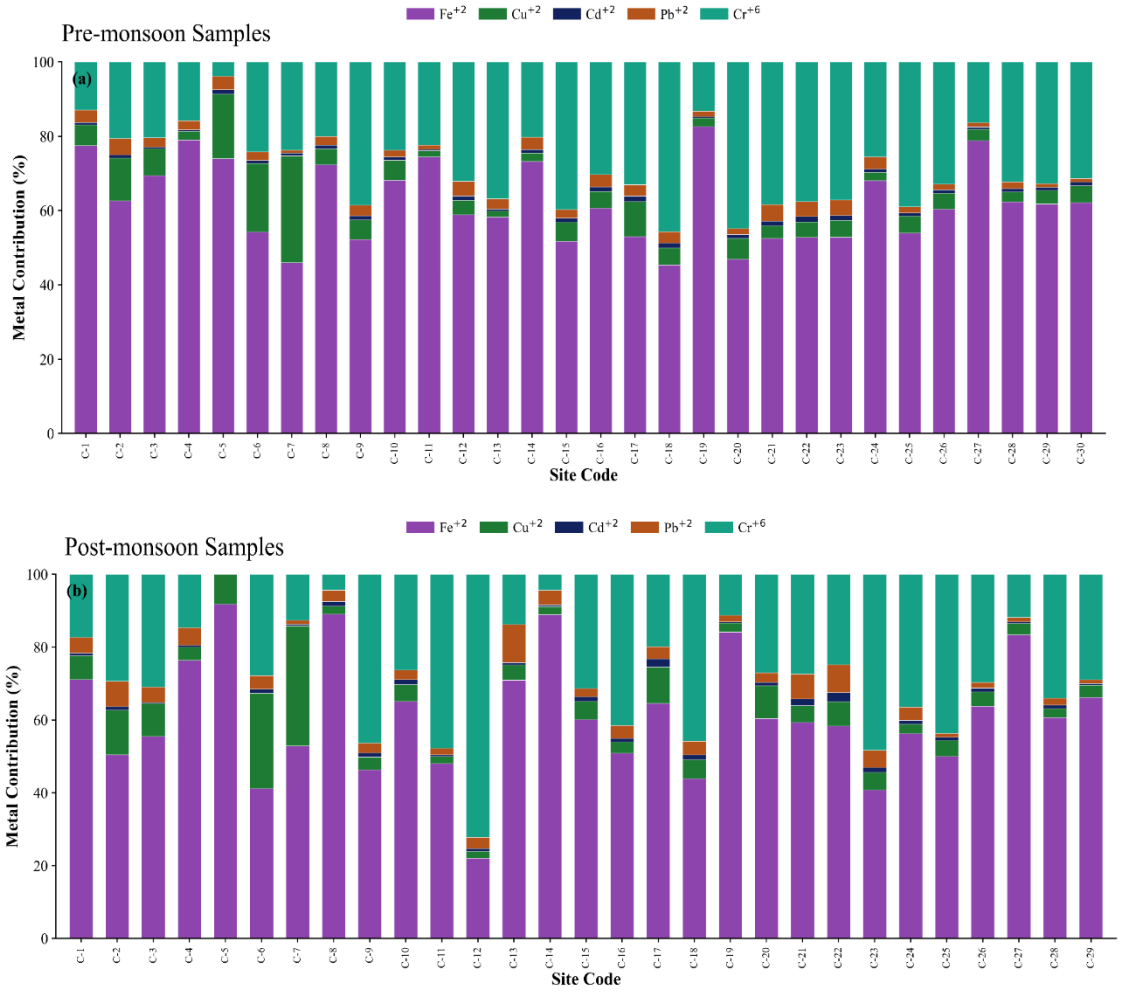

592

593 **Fig. 6** The percentage heavy metal content has been plotted for both seasons at all the sampling
594 locations.

595 The risk associated with the exposure of heavy metals through various routes (oral as well as
596 dermal) were computed using Chronic daily intake (CDI), Hazard quotient (HQ) and Total

hazard index (HI) to ensure compliance and assess human health impact. The CDI and HQ have been plotted in Fig 7.

The CDI values of heavy metals for dermal exposure reveals distinct ranges of exposure frequency and seasonal effects, CDI values for Cd ranges from 3.57×10^{-6} to 6.01×10^{-6} (for adults) and 1.05×10^{-5} to 1.77×10^{-5} (for children), Cr ranging from 2.86×10^{-5} to 7.72×10^{-4} (adults) and 8.43×10^{-5} to 2.28×10^{-3} (children), Cu ranges from 1.14×10^{-5} and 1.73×10^{-4} (adults) and 3.37×10^{-5} to 0.5×10^{-3} (children), Fe ranges from 1.60×10^{-4} to 1.22×10^{-3} (adults) and 0.4×10^{-3} to 0.3×10^{-3} (children) and Pb ranges from 4.14×10^{-7} to 3.86×10^{-6} (adults) and 1.22×10^{-6} to 1.39×10^{-5} (children). While oral ingestion of contaminated water shows significantly higher CDI values of Cd ranges from 7.54×10^{-4} to 1.27×10^{-3} (adults) and 2.88×10^{-3} to 4.84×10^{-3} (children), Cr ranges from 0.003 to 0.081 (adults) and 0.012 to 0.311 (children), Cu ranges 0.002 to 0.036 (adults) and 0.009 to 0.139 (children), Fe ranges 0.033 to 0.256 (adults) and 0.129 to 0.978 (children) and Pb values ranges from 0.0008 to 0.008 (adults) and 0.003 to 0.031 (children). Pb maintains comparatively lower values across both the routes but still shows higher oral exposure than dermal intake same as for different heavy metals. Overall, children continuously exhibit higher CDI values than adults for all elements and from both routes dermal as well as oral intake shows a greater vulnerability.

Additionally, the HQ values are specifically alarming for children during pre-monsoon season as values of Cr (mean: 41.30, surpasses the safe threshold) and Cd (mean: 7.56) via the oral route substantially exceeded the safe threshold of 1. Adults showed comparatively lower yet still concerning HQ values for Cr (mean: 10.82) and Cd (mean: 1.98), both crossing the threshold as well. During the post-monsoon season, these values were comparatively lower than those observed in pre-monsoon, with children recording HQ values of 23.28 for Cr and 4.23 for Cd, while adults showed 6.10 for Cr and 1.11 for Cd, though both groups continued to

exceed the safe limit. Pb also exceeded the safety threshold consistently across both seasons and demographic groups, with children showing HQ values of 8.35 (pre-monsoon) and 5.93 (post-monsoon), and adults recording 2.19 and 1.55, respectively, indicating a significant and persistent non-carcinogenic health risk associated with Cr, Cd, and Pb exposure through drinking water.

As reported by Vesković et al. (2024), the improper management of wastes and mining activities are mainly responsible for heavy metal pollution. Heavy metals like Cd and Cr can cause lungs or skin cancer or even other organ failures by their long-term exposure. These elements have tendency to bioaccumulate in food chain and transfer from one living things to another. Even, a small dose of Cd, can cause neurological dysfunction, kidney problem or even impact our reproductive system. We have analysed Cr (VI), most biologically toxic form of Cr, its exposure may cause disruption in normal working of cells and can induce genetical abnormalities (Mishra & Bharagava, 2016). It was observed that the HQ value for Cr and Pb were consistently high in pre- and post-monsoon season, mainly for children's. The oral pathway of exposure is found more dangerous than dermal pathway for all elements.

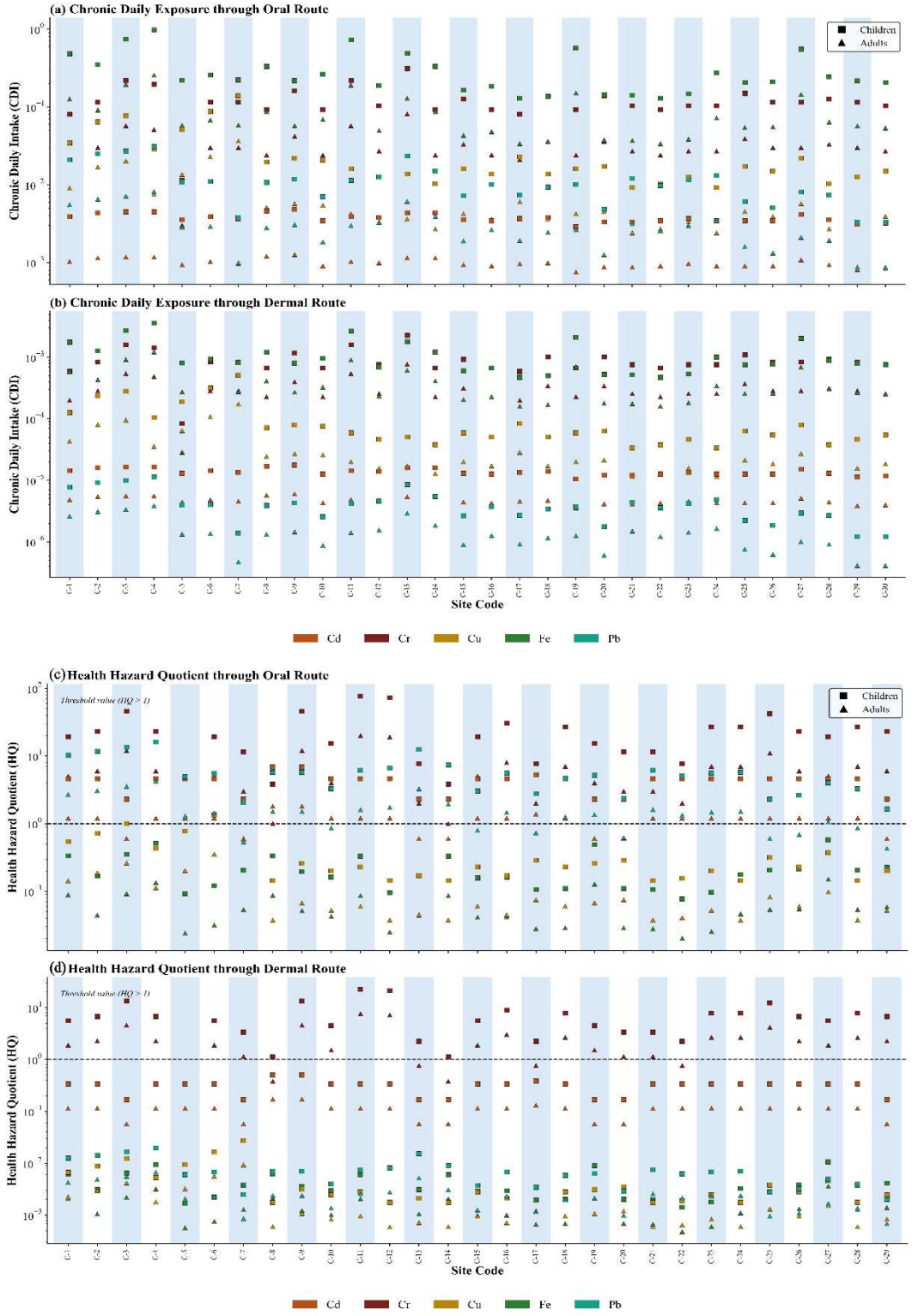

636

637 **Fig. 7 a) & b)** CDI values are plotted against sampling locations for pre-monsoon and post-
638 monsoon seasons. **c) & d)** HQ values are plotted against sampling locations for pre-monsoon
639 and post-monsoon seasons.

Hazard Index (HI) represents the combined effect of all heavy metals through oral pathways, and the results indicate significant seasonal and demographic variability are shown in Fig. 8. Among adults HI values ranging between 5.89 to 44.59 during pre-monsoon and from -1.31 to 30.81 during post-monsoon, negative values of HI during post-monsoon season showing a rounding artifact in one low concentration sample. Children showed markedly higher values ranging from 21.99 to 161.10 during pre-monsoon and from -4.12 to 110.90 during post-monsoon season, consistently two–three times greater than the corresponding adult values of nearby samples.

The threshold value of HI greater than 1 indicates potential health risk. Adults show 100 % of samples exceeding during pre-monsoon seasons that reduces to 97% during post-monsoon samples explains dilution from monsoonal recharge act to reduce the overall exposure level. The children showed a similar pattern with 100% sampling locations exhibiting severe risk that minimized to approximately 97% during post-monsoon, confirming that only seasonal recharge was not sufficient to reduce the risk for sensitive subgroups to safe limits. The values of HI or both adult and children are given in Supplementary Table S8.

These results are significantly demonstrating the demographic difference between adults and children with children being the most sensitive population across both seasons. This consistent elevated HI values for children even in post-monsoon season when dilution effect also acts to reduce the contamination load suggesting that natural seasonal hydrodynamic processes are insufficient to reduce the exposure risk to this sensitive subgroup.

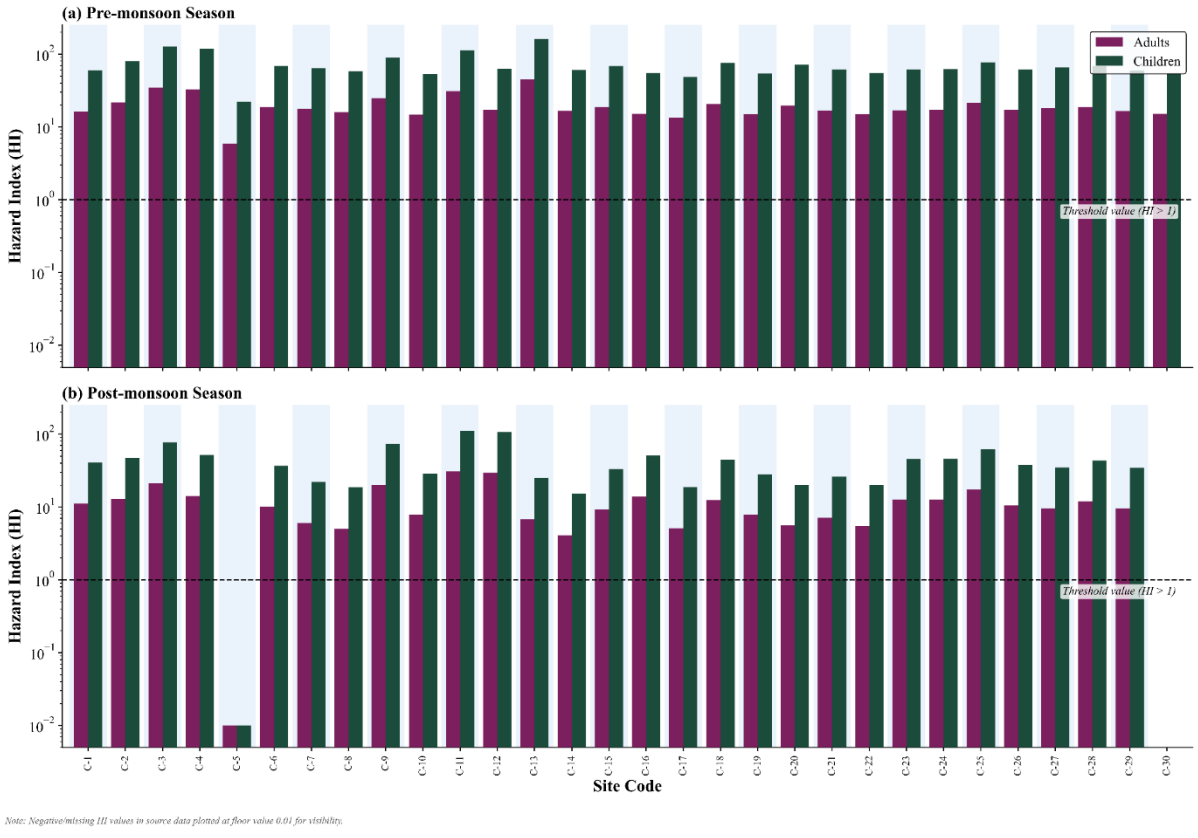

Fig. 8 Total Hazard Index (HI) values across sampling sites for children and adults during pre- and post-monsoon seasons.

4.5 Hydrogeochemical Variations due to Geogenic and anthropogenic controls

Principal component analysis (PCA) is the multivariate statistical technique used for dimensional reduction of datasets while preserving most of the variance. For groundwater quality assessment of complex systems of Khetri mine region, PCA helps identify the dominant geochemical processes and potential sources of contamination, whether geogenic (natural) or anthropogenic (human-induced). By analyzing correlations among numerous physicochemical and trace metal parameters, PCA can group variables with similar behavior and reveal the latent factors influencing groundwater chemistry, such as rock-water interaction, leaching from mine tailings, or agricultural runoff.

672 The findings demonstrated that the first five principal components, having (Eigen value>1),
673 cumulatively explain 70.80% of the total variance in the pre-monsoon and 72.04% in the post-
674 monsoon (Fig. 9). This clearly indicates a robust reduction in the dataset's dimensionality and
675 is helpful in identifying key controlling factors. Strong positive loadings of Ca^{+2}, Mg^{+2}, Cl^{-},
676 SO_4^{2-}, HCO_3^{-}, TDS, and EC are shown in PC1 of the pre-monsoon season (Supplementary
677 Table S6), which comprises 45.78% of the variance, strongly suggesting that natural geogenic
678 sources are the main key factors. The association of these ions indicates the dissolution of
679 carbonate minerals such as calcite ($CaCO_3$) and dolomite ($CaMg(CO_3)_2$ and evaporite minerals
680 like Gypsum ($CaSO_4.2H_2O$) and Anhydrite ($CaSO_4$) from the aquifer. High TDS and EC
681 loadings confirm that mineral dissolution is the primary driver of salinity and overall ionic
682 strength in the pre-monsoon season. The shift in the variance of PC1 (35.90%) in the post-
683 monsoon season (Supplementary Table S7) indicates recharge-enhanced geogenic processes
684 with anthropogenic mixing. The strong positive loading of Ca^{+2}, Mg^{+2}, HCO^{-}_3, TDS, and EC
685 reconfirms that there is a primary role of carbonate mixing. The strong incorporation of Cl^{-},
686 NO_3^{-}, and SO_4^{2-} reveals key seasonal changes that explain how monsoon rainfall not only
687 facilitates groundwater recharge and accelerates rock-water interaction but also facilitates the
688 movement of contaminants from the surface to the aquifers.

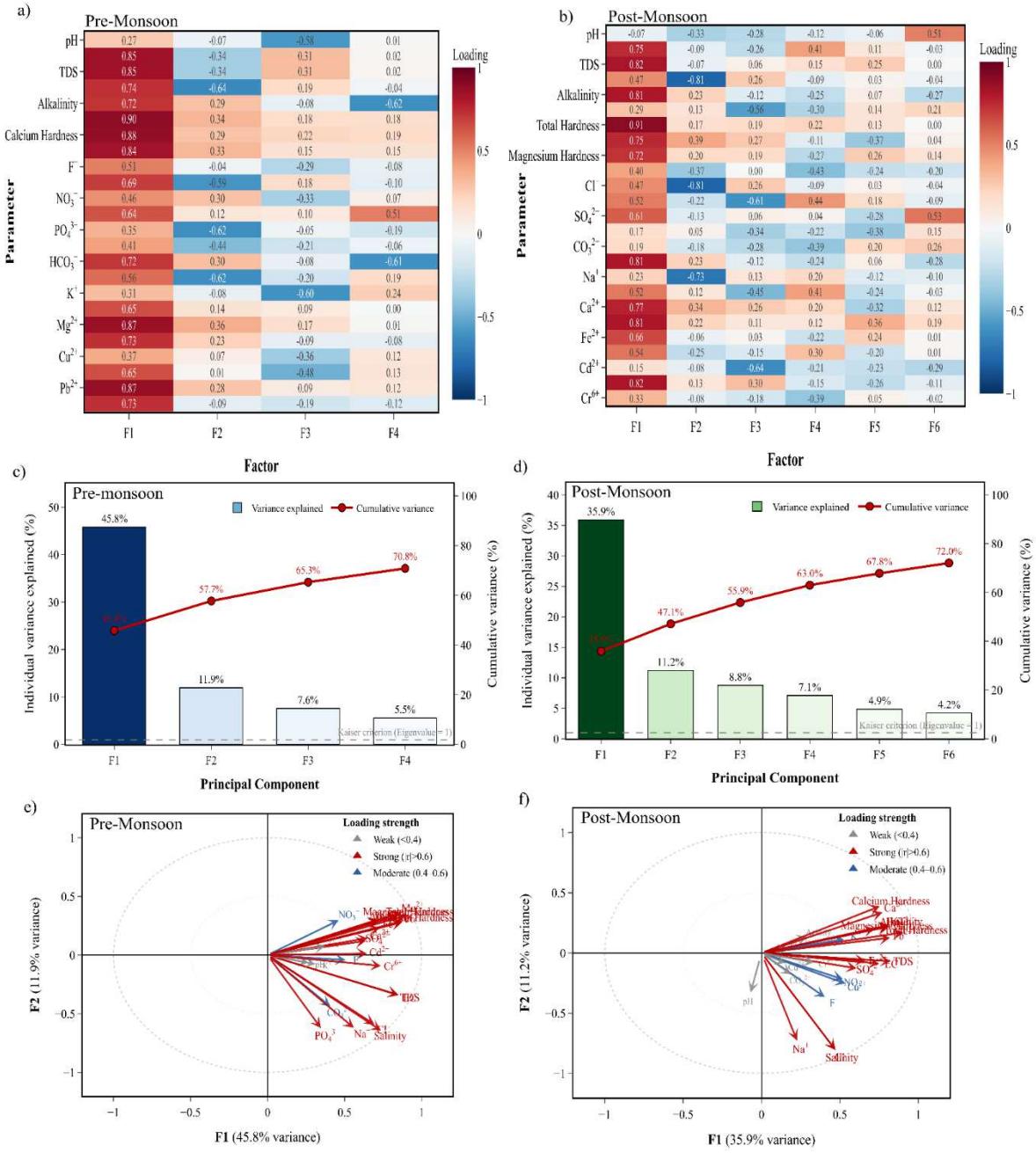

689

690 **Fig. 9** The heatmap of factors loading plot, scree plot and two-dimensional bivariate plot for
691 pre-monsoon and post-monsoon season.

692 The strong loading of Cl^- and NO_3^- in PC1 indicates that a mixing phenomenon is occurring,
693 where geogenic signatures are combining with anthropogenic overlays from surface runoff.
694 PC2 of the pre-monsoon season, accounting for 11.92% of the variance with high loadings of

Na^+, K^+, and NO_3^-, explains the contribution of anthropogenic activities. High loading of K^+ and NO_3^- identifies the role of agricultural practices. Na^+ and K^+ mainly come from the use of potassium-based fertilizers and the irrigational return flow process, while Nitrate generally comes from the leaching of chemical fertilizers and manures from the agricultural fields. A moderate inverse correlation between pH and these components suggests that it is mainly buffered by carbonate weathering processes and not significantly impacted by anthropogenic inputs. Inversely, during the post-monsoon season, a positive correlation is observed between pH and Na^+, K^+, F^-, and PO_4^{3-} in PC2 (11.20% variance), indicating that leachates from agriculture and pH buffering occur simultaneously. These ions serve as a reliable indicator of fertilizer application, along with phosphate ions. The positive loading of pH suggests that, due to recharge in the post-monsoon season. groundwater elevates the bicarbonate (HCO_3^-) level through high dissolution, which causes a buffering effect and helps raise the pH of the groundwater in the post-monsoon season. In the pre-monsoon season, the PC3 component shows a total variance of 7.57% with dominance of Cd, Cr, Pb, and F indicates the influence of heavy metals and industrial pollution. The co-occurrence of toxic heavy metals with fluoride shows the potential contribution of discharge coming from mining and metallurgical activities and leachates from the extensive use of herbicides and pesticides in agricultural processes. The movement of fluoride ions may also contribute to weathering of minerals (fluoride-bearing rock minerals) under specific geochemical conditions. In the post-monsoon season PC3 contributes to 8.75% of variance indicating dominance of Cd, Cr, Pb, and Cu confirms the mobilization and transport of heavy metals with rainfall. This may occur due to surface runoff of industrial waste or mining leachates or the rising water level due to rain, that may facilitate the subsurface leaching of these pollutants from the soil or mine tailings into the aquifer.

719 **PMF Model performance**

720 PMF with four factors gave most robust and interpretable for groundwater chemistry of both
721 seasons. Increment in factor count from three to four reduced Q(robust)/Q_exp from 2.61 to
722 2.17 in pre-monsoon season whereas it decreases from 3.66 to 3.34 in post-monsoon season.
723 The existing final solution had Q(robust) values 417.0 and 614.7 (Q_exp=192 and 184)
724 respectively and Q(true)/Q(robust) was 1.00, that clearly says not a single sample is responsible
725 for controlling the solution. Scaled residual fell between ±3 for 90-100% of samples of each
726 species. Major ions were nicely reproduced with observed vs predicted R^2 value reached 0.99
727 for SO_4^{2-} and 0.85 for HCO_3^-. Bootstrap factors were mapped to their base run counterparts in
728 81-100% of runs. DISP does not shows any swap at dQmax=4, except for pre-monsoon with
729 two swaps in F3. Non-zero FPEAK increased Q value without sharpening the factor profiles,
730 so the central solution was retained with FPEAK=0.

731 **Factors controlling groundwater chemistry**

732 Total four factors had resolved in each season that corresponds to different processes i.e.,
733 carbonate weathering, salinization, sulfide oxidation related to mining and agricultural inputs
734 (Fig 10). The chemical signature and the relative importance get changed with monsoon and
735 their shifting indicates how the aquifer will respond to recharge. Carbonate Weathering ((pre-
736 monsoon F1; post-monsoon F4) was found largest contributor for groundwater mineralization
737 that contributes 37.6% of TDS in pre-monsoon and 42.5% in the post-monsoon season. This
738 factor was defined by HCO_3^- ((63.9% and 60.1%) and Mg^{2+} (47.8% and 77.8%) ion which
739 reflects dissolution of carbonate and magnesium-rich silicate minerals in the host rocks. Its
740 sample wise contribution also increased with the calculated pCO_2 (($\rho = 0.68$ and 0.54, $p < 0.01$)
741 and dolomite saturation ($\rho = 0.50$ and 0.43) that is consistent with CO_2 driven weathering. In
742 post-monsoon season this factor was also carried most of the Cr^{+6} (83.4%). Chromium is mostly

found in mafic minerals and Cr (III) oxidizes to mobile Cr (VI) under the oxic conditions produced due to recharge. This attribution is, however, poorly constrained (DISP range 0-83.8%). Salinization factor (pre-monsoon F2; post-monsoon F1) was dominated by Cl^- ion (88.1% and 60.7%) and Na^+ ion (58.8% and 65.8%). It measures the evaporative concentration of groundwater under the semi-arid climate along with number of leached salts get stored in the unsaturated zone. Its contribution to TDS fell from 38.8% in pre-monsoon to 24.2% in post-monsoon, the largest seasonal change of any source found, which shows the diluting effect of recharge. The strong positive correlation of this factor with halite saturation in both seasons (ρ = 0.75 and 0.71, $p < 0.01$) supports this result. Halite remained highly undersaturated throughout pre-monsoon and post-monsoon seasons (median SI ≈ -5.5), so Na^+ and Cl^- accumulated freely rather than being limited by mineral precipitation. Sulfide oxidation related to mining (pre-monsoon F4; post-monsoon F2) is the most important factor for understanding the effect of copper mining process as in the monsoon it accounted for 69.6% of SO_4^{2-}, with Pb^{2+} (35.8%) and TH (41.2%), and it was the best-constrained factor in the solution: 100% bootstrap mapping, no DISP swaps, and a bootstrap interval for SO_4^{2-} of only 61.0-79.0%. The co-occurrence of sulfate and lead points to oxidation of the pyrite, chalcopyrite and galena that make up the Khetri ore assemblage. After the monsoon the factor retained its SO_4^{2-} (50.3%) and Pb^{2+} (51.6%) loadings but also carried 69.6% of Ca^{2+}. The addition of calcium is the expected geochemical signature of sulfuric acid being neutralized by carbonate minerals ($CaCO_3 + H_2SO_4 \rightarrow Ca^{2+} + SO_4^{2-} + H_2O + CO_2$). This source contributed almost the same share of TDS in both seasons (23.7% and 23.8%), and the same group of wells (samples 1, 2, 3, 13, 14 and 24) received the largest contributions in both. The mine-drainage signal is therefore spatially persistent rather than episodic. Agricultural input (pre-monsoon F3; post-monsoon F3) is defined mainly by NO_3^-. Before the monsoon, nitrate was split between this factor (47.0%) and the carbonate-weathering factor (47.2%), and the factor also carried 45.4% of

768 Cu^{2+}, suggesting a mixed anthropogenic source. This pre-monsoon factor was the least stable
769 in the solution, so its interpretation is tentative. After the monsoon the agricultural signal
770 became much more distinct: 96.1% of NO_3^- was assigned to F3, together with 61.4% of Cd^{2+}
771 and 50.2% of F^-. The NO_3^-–Cd^{2+}–F^- association is characteristic of phosphate fertilizers, in
772 which Cd and F occur as impurities. It indicates that fertilizer residues stored in soils are flushed
773 into the aquifer by monsoon infiltration. In both seasons this factor showed no relationship with
774 mineral saturation, as expected for a surface-derived, non-geogenic source.

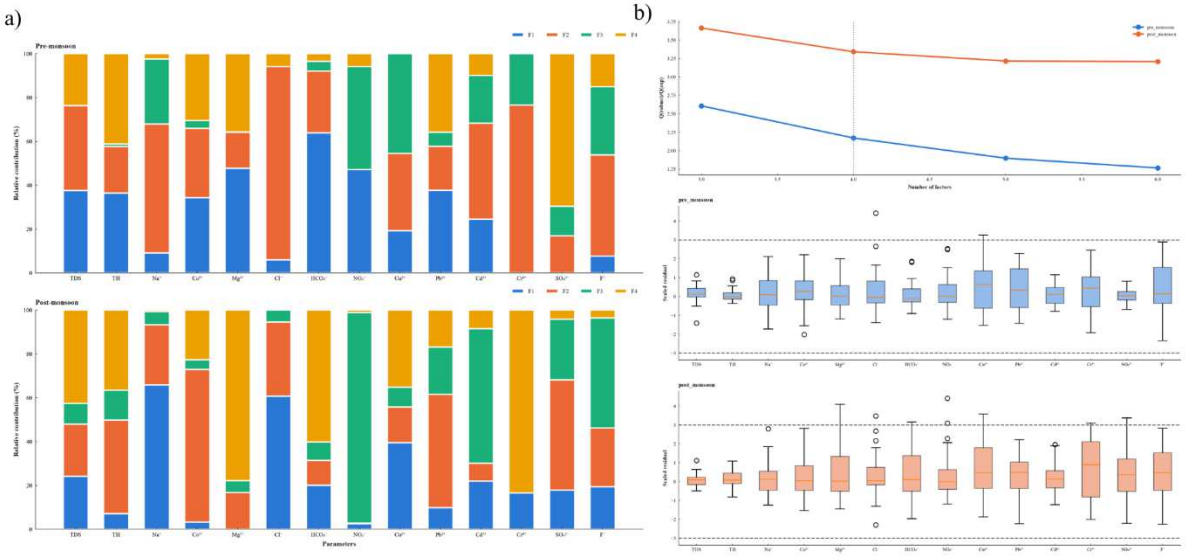

775

776 **Fig. 10** PMF Factorization for factor contribution and b) Diagnostic test for PMF for pre and
777 post-monsoon seasons.

778 **Monsoon recharge and near-neutral mine drainage**

779 The seasonal variation in the PMF profiles and the saturation indices collectively describes
780 how much aquifer reacts to recharge. In the pre-monsoon season, the groundwater was found
781 heavily mineralised with carbonate saturated system as calcite SI varies from +0.60 to +1.72
782 in all the samples and HCO_3^- ion (median 2464 mg/L). Salinization and carbonate weathering

783 were collectively contributed to 76% of total dissolved solids. Recharge after monsoon diluted
784 the salinity signal and decreases bicarbonate content (median 860 mg/L) and pH (from median
785 7.1 to 6.8). It also takes the aquifer to calcite equilibrium (median SI -0.09; 25 samples within
786 ±0.5). During this whole period of transition, SO_4^{2-} remained highly concentrated (up to 3457
787 mg L^{-1}) and all the samples of both seasons stayed undersaturated with respect to gypsum
788 indicates dissolved sulfate is mainly controlled by continuing supply not by mineral solubility.
789 The contribution of sulfate-oxidation factor is closely correlated with gypsum saturation in both
790 pre- and post-monsoon season ($\rho = 0.93$, $p < 0.01$). Based on well-to-well comparison, it was
791 found that wells receiving more mine derived sulfate approaches towards gypsum saturation.
792 In the post-monsoon season the same well was also found correlated with calcite saturation (ρ
793 = 0.44) and fluorite saturation ($\rho = 0.49$), that reflects Ca^{+2} released with carbonate neutralizes
794 acidity. The high order of pCO_2 by two to three times above atmospheric levels (median $10^{-0.91}$
795 atm) was found consistent with the same neutralization reaction. These findings highlight that
796 sulfide oxidation in copper mining region produces near-neutral mine drainage rather than
797 classic acid mine drainage. Acidity caused due to oxidation of ore and waste material is mostly
798 consumed by the carbonate-rich aquifer, so pH stays in between range of 5.98 and 7.94. This
799 chemical footprint of mining is instead a persistent sulfate-lead signal, together with calcium
800 released by neutralization. Monsoon recharge does not dilute this signal away. Instead, it
801 mobilizes oxidation products stored in the unsaturated zone and progressively consumes the
802 aquifer's carbonate buffering capacity. Over time, continued oxidation combined with loss of
803 buffering could lower pH and increase metal mobility, especially in the wells nearest the mine
804 workings, where the sulfide-oxidation factor is strongest. Confirming the sulfide origin of the
805 sulfate, as opposed to dissolution of evaporitic gypsum, would require sulfur isotope analysis
806 ($\delta^{34}S–SO_4^{2-}$). This is recommended for future monitoring.

807 **Conclusion**

An overall assessment of groundwater samples from the Khetri copper mining region, Jhunjhunu, Rajasthan, India, was carried out. This study included hydrogeochemical evaluation, groundwater quality assessment using EWQI, mineral saturation index calculation and non-carcinogenic health risk assessment due to exposure of heavy metal contaminated groundwater through oral as well as dermal pathways were accessed for adults as well as children. The main finding of this study includes:

1. This study reveals groundwater samples are slightly acidic to alkaline in nature. The overall dominance pattern of major cations and anions was $Mg^{2+} > Ca^{2+} > Na^{+} > K^{+}$ during pre-monsoon season and $Na^{+} > Mg^{2+} > Ca^{2+} > K^{+}$ in post-monsoon season.
2. Piper Diagram reveals a clear shift from heterogeneous mixed-type composition of groundwater samples (Ca^{2+}-Mg^{2+}-HCO_3^{-}, Ca^{2+}-Mg^{2+}-Cl^{-}-SO_4^{2-}, and Na^{+}-Cl^{-}-SO_4^{2-}) reflecting mixed geogenic control of carbonate dissolution, silicate weathering and minor evapourite/ anthropogenic inputs under low water-table condition in the pre-monsoon season to homogenous Na^{+}-HCO_3^{-} dominant facies type in post monsoon due to monsoonal recharge, cation exchange and silicate weathering. Gibb's plot illustrates rock-water interactions as the dominant control on groundwater chemistry, with most of the pre- and post-monsoon samples falling in rock-water dominance across both seasons.
3. The hydro geochemistry of groundwater samples was controlled by calcite and dolomite dissolution, cation exchange, reverse ion-exchange and evaporite dissolution. The scattered plots between $Ca^{2+} + Mg^{2+}$ versus $SO_4^{2-} + HCO_3^{-}$ indicates carbonate weathering in pre-monsoon and shift towards silicate weathering in post-monsoon. Na^{+} versus Cl^{-} shows halite dissolution, $Ca^{2+} + Mg^{2+}$ vs total cations indicate calcite and dolomite dissolution.

4. EWQI shows that 90% of samples fall into the Extremely Poor category with EWQI greater than 200 in the pre-monsoon season and found that the interaction between fractured schist-quartzite formations is responsible for enhanced contamination transport and localised limestone or gneissic zones are reducing the contamination.
5. This consistent elevated HI values for children even in the post-monsoon season when dilution effect acts to reduce the contamination load suggesting that natural seasonal hydrodynamic processes are insufficient to reduce the exposure risk to this sensitive subgroup.
6. Geochemical modeling (PHREEQC) demonstrates a seasonal transition from carbonate and fluorite supersaturation to near-equilibrium alongside elevated pCO_2 confirming that monsoon recharge consumes aquifer alkalinity to neutralize sulfide oxidation acidity. Furthermore, persistent gypsum and halite undersaturation across both seasons indicates that dissolved SO_4^{2-}, Na^+, Cl^- are governed by ongoing source inputs and evaporative-recharge dynamics rather than mineral precipitation limits.
7. Seasonal PMF modeling resolved four persistent processes: carbonate weathering, salinization, sulfide oxidation, and agricultural return flow showing that monsoon recharge controls aquifer mineralization by diluting salts, flushing stored agrochemicals, and mobilizing mine drainage. Crucially, the stable mining factor reveals that carbonate minerals currently buffer acidity into near-neutral mine drainage, though ongoing oxidation threatens this long-term buffering capacity.

In conclusion, the findings highlight a pressing public health concern in the Khetri mining region. There is an urgent need for effective groundwater monitoring programs, pollution source control measures, and remediation strategies. Moreover, raising community awareness, promoting alternative safe water sources, and formulating region-specific water management policies should be prioritized. This integrated

methodological approach adopted in this study serves as a model for similar mining-affected regions facing groundwater contamination challenges across India and other parts of the world.

Acknowledgement

The authors would like to acknowledge the Environmental Biology Laboratory, Department of Zoology, Patna University, for providing the necessary facilities for physicochemical analysis of samples.

Author contributions

Bhavya Swami: Conceptualization, investigation, Analysis, writing original draft, and analysis; **Manish Kumar:** Analysis, Methodology, reviewing, and editing; **Emmanuel Danoba Sunkari:** Review and Editing; **Rajesh Kumar:** Supervision, reviewing, and editing; **Anupma Kumari:** Supervision, reviewing, and editing; **Ramesh Kumar:** Supervision, reviewing, and editing

Funding

No funding

Ethics declarations

Conflict of interest

The authors declare no competing interests associated with this publication.

Ethical approval

Not applicable.

Data availability

Data will be made available upon reasonable request from the corresponding author.

References

1. America, I., Zhang, C., Werner, A. D., & van der Zee, S. E. (2020). Evaporation and salt accumulation effects on riparian freshwater lenses. *Water Resources Research*, *56*(12), e2019WR026380.
2. Adnan, M., Xiao, B., Ali, M. U., Xiao, P., Zhao, P., Wang, H., & Bibi, S. (2024). Heavy metals pollution from smelting activities: A threat to soil and groundwater. *Ecotoxicology and Environmental Safety*, *274*, 116189.
3. Ali, H., Khan, E., & Ilahi, I. (2019). Environmental chemistry and ecotoxicology of hazardous heavy metals: environmental persistence, toxicity, and bioaccumulation. *Journal of chemistry*, *2019*(1), 6730305.
4. Alizadeh Z, Yazdi J, Moridi A (2018) Development of an entropy method for groundwater quality monitoring network Design. Environ Process 5(4):769-788.
5. Anjali, N., Sabitha, A. R., Achu, A. L., Aju, C. D., & Gopinath, G. (2025). Hydrogeochemical processes and physicochemical parameters controlling the groundwater chemistry of a tropical river basin, Southern India. Discover Geoscience, 3(1), 204.
6. Arkoc O, Ucar S, Ozcan C (2016) Assessment of impact of coal mining on ground and surface waters in Tozakl coal field, Krklareli, northeast of Thrace, Turkey. Environ Earth Sci 75(6):1-13.
7. Atkins, A. S., & Pooley, F. D. (1982). The effects of biomechanisms on acidic mine drainage in coal mining. International journal of mine water, 1(1), 31-44.
8. Bade, R., Oh, S., Shin, W. S., & Hwang, I. (2013). Human health risk assessment of soils contaminated with metal (loid) s by using DGT uptake: A case study of a former Korean metal refinery site. Human and Ecological Risk Assessment: An International Journal, 19(3), 767-777.
9. Barman, J., Biswas, B., & Soren, D. D. L. (2025). Groundwater trend analysis and regional groundwater drought assessment of a semi-arid region of Rajasthan, India. *Environment, Development and Sustainability*, *27*(2), 3415-3439.

10. Benneyworth, L., Gilligan, J., Ayers, J. C., Goodbred, S., George, G., Carrico, A., ... & Piya, B. (2016). Drinking water insecurity: water quality and access in coastal south-western Bangladesh. *International journal of environmental health research*, *26*(5-6), 508-524.
11. Briffa, J., Sinagra, E., & Blundell, R. (2020). Heavy metal pollution in the environment and their toxicological effects on humans. *Heliyon*, *6*(9).
12. Chakraborty, R., & Gupta, H. (2024). Impact of opencast mining on soil physico-chemical properties-A case study from bansra OCP of Raniganj coalfield. International Journal of Ecology and Environmental Sciences, 50(5), 777-791.
13. Chen, J., Chen, M., Yang, W., Gan, L., Owens, G., & Chen, Z. (2025). Mathematical modeling of in situ synthesis of metal sulfides by sulfate-reducing bacteria and treatment of acidic mine drainage. *Chemical Engineering Journal*, 167683.
14. Chu, X., Meng, Y., Wang, Y., Du, Z., Wang, L., & Liang, T. (2026). Source-sink relationships and health risk assessment of heavy metals in farmland soils of a Southwest Karst Industrial cluster: based on PMF and Monte Carlo simulation. *Environmental Geochemistry and Health*, *48*(6), 256.
15. Dashora, M., Kumar, A., Kumar, S., Kumar, P., Kumar, A., & Singh, C. K. (2022). Geochemical assessment of groundwater in a desertic region of India using chemometric analysis and entropy water quality index (EWQI). Natural Hazards, 112(1), 747-782.
16. Dai, D. K., & Zhou, J. (2025). Spatial distribution and risk assessment of heavy metal contamination in soil-crop systems near gold mining areas. *Environmental Geochemistry and Health*, *47*(6), 191.
17. Dávila-Cisneros, S., Castañeda-Miranda, A. G., Bautista-Capetillo, C. F., Mattos-Villarroel, E. D., Rodríguez-Abdala, V. I., Rovelo, C. O. R., ... & Delgado, S. I. (2026). Monitoring the adverse effects of mining on water resources: A review using remote sensing, geographic information systems, and artificial intelligence. *Physics and Chemistry of the Earth, Parts A/B/C*, 104380.
18. El Amari, K., Valera, P., Hibti, M., Pretti, S., Marcello, A., & Essarraj, S. (2014). Impact of mine tailings on surrounding soils and ground water: Case of Kettara old mine, Morocco. *Journal of African Earth Sciences*, *100*, 437-449.

19. Foster, S., Pulido-Bosch, A., Vallejos, Á. *et al.* Impact of irrigated agriculture on groundwater-recharge salinity: a major sustainability concern in semi-arid regions. *Hydrogeol J* **26**, 2781-2791 (2018).
20. Fida, M., Li, P., Ning, J., Khorshed Alam, S. M., & Wang, Y. (2025). Groundwater nitrate contamination around a municipal landfill: hydrogeochemical insights, source identification, and health risk assessment. *Environmental Geochemistry and Health*.
21. Gibbs, R. J. (1970). Mechanisms controlling world water chemistry. *Science, 170*(3962), 1088-1090.
22. Giljum, S., Maus, V., Sonter, L., Luckeneder, S., Werner, T., Lutter, S., ... & Bebbington, A. (2025). Metal mining is a global driver of environmental change. Nature Reviews Earth & Environment, 1-15.
23. Gorgij AD, Kisi O, Moghaddam AA, Taghipour A (2017) Groundwater quality ranking for drinking purposes, using the entropy method and the spatial autocorrelation index. Environ Earth Sci 76(7):269.
24. Guettaia, S., Boudjema, A., Derdour, A., Laoufi, A., Almohamad, H., Al-Mutiry, M., & Abdo, H. G. (2025). Hydrochemical Characterization and Predictive Modeling of Groundwater Quality in Karst Aquifers Under Semi-Arid Climate: A Case Study of Ghar Boumaaza, Algeria. Sustainability, 17(15), 6883.
25. Gupta, P., Guha, D. B., & Chattopadhyay, B. (1998). Basement-cover relationship in the Khetri copper belt and the emplacement mechanism of the granite massifs, Rajasthan, India. Journal Geological Society of India, 52(4), 417-432.
26. Hamma, B., Bekkouche, M. F., Bouaicha, F., Elnagdy, K. A., Alzaed, A., Barkat, A., ... & Hussein, E. E. (2025). Hydrogeochemical assessment of groundwater for agricultural suitability in the Ksour Mountains, Algeria. *Scientific Reports*, *15*(1), 36441.
27. Hasan, M. F., Smith, R., Vajedian, S., Pommerenke, R., & Majumdar, S. (2023). Global land subsidence mapping reveals widespread loss of aquifer storage capacity. *Nature Communications*, *14*(1), 6180.
28. He, S., & Wu, J. (2019). Relationships of groundwater quality and associated health risks with land use/land cover patterns: a case study in a loess area, northwest China. *Human and Ecological Risk Assessment: An International Journal*, *25*(1-2), 354-373.
29. Huang PH, Chen J (2012) Recharge sources and hydrogeochemical evolution of groundwater in the coal-mining district of Jiaozuo, China. Hydrogeol J 20(4):739-754.

30. Holzheid, A., Zhao, H., Cabus, T., Fan, L., Kuhn, T., Sun, L., ... & Zhang, Y. (2024). Deep-sea mining of massive sulfides: Balancing impacts on biodiversity and ecosystem, technological challenges and law of the sea. Marine Policy, 167, 106289.
31. IS10500, BIS (2012). *Indian standard drinking water-specification (second revision)* (pp. 1-11). New Delhi: Bureau of Indian Standards (BIS).
32. Ikpi, G. E., Nganje, T. N., Edet, A., Adamu, C. I., & Eyong, G. A. (2024). Investigation of hydrochemical characteristic, water quality and associated health risks of metals and metalloids in water resources in the vicinity of Akamkpa quarry district, southeastern, Nigeria. *Geochemical Transactions*, *25*(1), 7.
33. Isah, A., Ojo, O. A., Kolawole, T. O., & Akinbiyi, O. A. (2026). Seasonal heavy metal mobilization in a tropical artisanal mining system: a source-to-receptor assessment. *Environmental Science and Pollution Research*, 1-21.
34. Jia, H., & Qian, H. (2025). Groundwater nitrate response to hydrogeological conditions and socioeconomic load in an agriculture dominated area. *Scientific Reports*, *15*(1), 1315.
35. Janardhanan, S., Nair, A. S., Indu, J., Pagendam, D., & Kaushika, G. S. (2023). Estimation of groundwater storage loss for the Indian Ganga Basin using multiple lines of evidence. *Scientific Reports*, *13*(1), 1797.
36. Jasechko, S., Seybold, H., Perrone, D., Fan, Y., Shamsudduha, M., Taylor, R. G., ... & Kirchner, J. W. (2024). Rapid groundwater decline and some cases of recovery in aquifers globally. *Nature*, *625*(7996), 715-721.
37. Karandish, F., Liu, S., & de Graaf, I. (2025). Global groundwater sustainability: A critical review of strategies and future pathways. *Journal of Hydrology*, *657*, 133060.
38. Kan, X., Dong, Y., Feng, L., Zhou, M., & Hou, H. (2021). Contamination and health risk assessment of heavy metals in China's lead–zinc mine tailings: A meta–analysis. *Chemosphere*, *267*, 128909.
39. Karki, R., Khan, A. A., Gara, S. K., Kumar, P., & Wadhwa, S. (2026). Assessing Mining-Induced Groundwater Level Decline Using Integrated Spatial and Statistical Techniques in the Moher Sub-basin, Singrauli Coalfield, India. *Mine Water and the Environment*, 1-17.
40. Khan, I., Singh, A., & Jamal, Y. (2025). Hydrogeochemical Dynamics of Groundwater in the Punjab Region of the Indo-Gangetic Plains: An Entropy-Weighted and Geochemical Modeling Approach. Earth Systems and Environment, 1-24.

41. Krishna Kumar, S., Hari Babu, S., Eswar Rao, P., Selvakumar, S., Thivya, C., Muralidharan, S., & Jeyabal, G. (2017). Evaluation of water quality and hydrogeochemistry of surface and groundwater, Tiruvallur District, Tamil Nadu, India. *Applied Water Science*, *7*(5), 2533-2544.
42. Kumar, R., Kumar, M., Kumar, R., Garg, V., Kumar, A., & Pippal, P. S. (2025). Assessment of fluoride and nitrate contamination in groundwater and their health implications in the marble City of Kishangarh, Rajasthan, India. Journal of Umm Al-Qura University for Applied Sciences, 1-15.
43. Kumar, R., Kumari, A., Kumar, R., Sulaiman, M. A., Zafar, M. M., Singh, A., ... & Pippal, P. S. (2023). Assessing the geochemical processes controlling groundwater quality and their possible effect on human health in Patna, Bihar. Environmental Science and Pollution Research, 30(49), 107138-107157.
44. Kundzewicz, Z. W. (2009). Water resources for sustainable development. *Hydrological Sciences Journal*, *42*(4), 467-480.
45. Li, W., Xu, B., Song, Q., Liu, X., Xu, J., & Brookes, P. C. (2014). The identification of 'hotspots' of heavy metal pollution in soil-rice systems at a regional scale in eastern China. Science of the Total Environment, 472, 407-420.
46. Liu, Z., Wang, X., Wan, X., Jia, S., & Mao, B. (2024). Evolution origin analysis and health risk assessment of groundwater environment in a typical mining area: Insights from water-rock interaction and anthropogenic activities. *Environmental Research*.
47. Li, Z., Ma, Z., van der Kuijp, T. J., Yuan, Z., & Huang, L. (2014). A review of soil heavy metal pollution from mines in China: pollution and health risk assessment. *Science of the total environment*, *468*, 843-853.
48. Loaiciga, H. A., & Doh, R. (2024). Groundwater for people and the environment: a globally threatened resource. *Groundwater*, *62*(3), 332-340.
49. Luo, C., Routh, J., Dario, M., Sarkar, S., Wei, L., Luo, D., & Liu, Y. (2020). Distribution and mobilization of heavy metals at an acid mine drainage affected region in South China, a post-remediation study. *Science of the Total Environment*, *724*, 138122.
50. Laoye, B., Olagbemide, P., Ogunnusi, T., & Akpor, O. (2025). Heavy metal contamination: sources, health impacts, and sustainable mitigation strategies with insights from Nigerian case studies. *F1000Research*, *14*, 134.
51. Mishra, S., & Bharagava, R. N. (2016). Toxic and genotoxic effects of hexavalent chromium in environment and its bioremediation strategies. *Journal of Environmental Science and Health, Part C*, *34*(1), 1-32.

52. Mititelu, M., Neacșu, S. M., Busnatu, Ș. S., Scafa-Udriște, A., Andronic, O., Lăcraru, A. E., ... & Olteanu, G. (2025). Assessing heavy metal contamination in food: implications for human health and environmental safety. Toxics, 13(5), 333.
53. Monir, M. M., & Sarker, S. C. (2024). Analyzing post-2000 groundwater level and rainfall changes in Rajasthan, India, using well observations and GRACE data. *Heliyon*, *10*(2).
54. Nazari, S., Reinecke, R., & Moosdorf, N. (2025). Global estimates of groundwater withdrawal trends and uncertainties. *Environmental Research Letters*, *20*(9), 094043.
55. Nasrabadi, T., & Abbasi Maedeh, P. (2014). Groundwater quality assessment in southern parts of Tehran plain, Iran. Environmental earth sciences, 71(5), 2077-2086.
56. Narayanan, M. S. S., Pitchaimani, V. S., Sivakumar, M., Dinesh Kumar, T., Abishek, S. R., & Karuppannan, S. (2025). Spatial assessment of heavy metal contamination in groundwater in the Kadaladi region, Tamil Nadu, India. *Scientific reports*, *15*(1), 27704.
57. Organization, W. H. Guidelines for drinking-water quality: first addendum to the fourth edition. (2017).
58. Pande, C. B., Tolche, A. D., Egbueri, J. C., Mohd Sidek, L., Singh, R., Mishra, A. P., ... & Sammen, S. S. (2025). Implications of seasonal variations of hydrogeochemical analysis using GIS, WQI, and statistical analysis method for the semi-arid region. Applied Water Science, 15(4), 80.
59. Panwar, S., Yang, S., Ray, E., Singh, P., Uniyal, S., & Paul, D. (2025). Deciphering dissolved load geochemistry of the Upper Ganga Basin: Natural weathering vs human impact. Journal of Geochemical Exploration, 272, 107702.
60. Piper, A. M. (1944). A graphic procedure in the geochemical interpretation of water-analyses. *Eos, Transactions American Geophysical Union, 25*(6), 914-928.
61. Punia, A., & Siva Siddaiah, N. (2017). Assessment of heavy metal contamination in groundwater of Khetri copper mine region, India and health risk assessment. *Asian Journal of Water, Environment and Pollution*, *14*(4), 9-19.
62. Punia, A., & Siddaiah, N. S. (2019). Mobility and behaviour of metals in copper mine tailings and soil at Khetri, India. *Mine Water and the Environment*, *38*(2), 385-390.
63. Punia, A., Joshi, P. K., & Siddaiah, N. S. (2021). Characterizing Khetri copper mine environment using geospatial tools. SN Applied Sciences, 3(2), 174.

64. Piwowarska, D., Kiedrzyńska, E., & Jaszczyszyn, K. (2024). A global perspective on the nature and fate of heavy metals polluting water ecosystems, and their impact and remediation. *CritiCal reviews in environmental sCienCe and teChnology*, *54*(19), 1436-1458.
65. Prusty, P., Mohakud, S. K., Mandal, A. R., Parray, K. A., & Farooq, S. H. (2026). Assessment of Heavy Metal Contaminations in Groundwater and Surface Water Resources of Sukinda Valley, Odisha, India. *Geological Journal*, *61*(2), 275-289.
66. Perez, N., Singh, V., Ringler, C., Xie, H., Zhu, T., Sutanudjaja, E. H., & Villholth, K. G. (2024). Ending groundwater overdraft without affecting food security. *Nature Sustainability*, *7*(8), 1007-1017.
67. Qiao X, Li G, Li M, Zhou J, Du J, Du C, Sun Z (2011) Influence of coal mining on regional karst groundwater system: a case study in West Mountain area of Taiyuan City, northern China. Environ Earth Sci 64(6):1525-1535.
68. Qu S, Wang GC, Shi ZM, Xu QY, Guo YY, Ma L, Sheng YZ (2018) Using stable isotopes (δD, $\delta^{18}O$, $\delta^{34}S$ and $^{87}Sr/^{86}Sr$) to identify sources of water in abandoned mines in the Fengfeng coal mining district, northern China. Hydrogeol J 26(5):1443-1453.
69. Rohde, M. M., Albano, C. M., Huggins, X., Klausmeyer, K. R., Morton, C., Sharman, A., ... & Stella, J. C. (2024). Groundwater-dependent ecosystem map exposes global dryland protection needs. *Nature*, *632*(8023), 101-107.
70. Singh, V., Karan, S. K., Singh, C., & Samadder, S. R. (2023). Assessment of the capability of SWAT model to predict surface runoff in open cast coal mining areas. *Environmental Science and Pollution Research*, *30*(14), 40073-40083.
71. Sarkar, S. C., & Dasgupta, S. (1980). Geologic setting, genesis and transformation of sulfide deposits in the northern part of Khetri copper belt, Rajasthan, India—an outline. Mineralium Deposita, 15(2), 117-137.
72. Shannon CE (1948) A mathematical theoryof communication. Bell Syst Tech J 27:379-423.
73. Shi WH, Yang TH, Yu QL, Li Y, Liu HL, Zhao YC (2017) A study of water-inrush mechanisms based on geo-mechanical analysis and an in-situ groundwater investigation in the Zhongguan iron mine. China Mine Water Environ 36(3):409-417.
74. Siame, T., Muzandu, K., Kataba, A., Weisiyu, Q., & M'kandawire, E. (2024). A comparative assessment of Lead (Pb) concentration and physicochemical parameters in

groundwater from the Kabwe mine and Lusaka non-mine sites, Zambia. *Discover Environment*, *2*(1), 101.

75. Singh, U. K., Ramanathan, A. L., & Subramanian, V. (2018). Groundwater chemistry and human health risk assessment in the mining region of East Singhbhum, Jharkhand, India. *Chemosphere*, *204*, 501-513.

76. Srinivasamoorthy, K., Chidambaram, S., Prasanna, M. V., Vasanthavihar, M., Peter, J., & Anandhan, P. (2008). Identification of major sources controlling groundwater chemistry from a hard rock terrain-a case study from Mettur taluk, Salem district, Tamil Nadu, India. *Journal of Earth System Science*, *117*(1), 49-58.

77. Su H, Kang W, Xu Y, Wang J (2017) Assessment of groundwater quality and health risk in the oil and gas field of Dingbian County, Northwest China. Expos Health 9(4):227-242.

78. Sun WJ, Zhou WF, Jiao J (2016) Hydrogeological classification and water inrush accidents in China's coal mines. Mine Water Environ 35(2):214-220.

79. Sui WH, Liu JY, Yang SG, Chen ZS, Hu YS (2011) Hydrogeological analysis and salvage of a deep coalmine after a groundwater inrush. Environ Earth Sci 62(4):735-749.

80. Subba Rao N, Sunitha B, Adimalla N, Chaudhary M (2020) Quality criteria for groundwater use from a rural part of Wanaparthy District, Telangana State, India, through ionic spatial distribution (ISD), entropy water quality index (EWQI) and principal component analysis (PCA). Environ Geochem Health 42(2):579-599.

81. Sulaiman, M. B., Adamu, A. M., Ali, S. B., Ezenobi, U. V., Gimba, A. M., Akinlotan, O. O., & Abubakar, A. (2024). Heavy metal contamination in medicinal plants: assessing carcinogenic and non-carcinogenic health risks. Discover Environment, 2(1), 11.

82. Tanwar, D., Tyagi, S., & Sarma, K. (2025). Seasonal and spatial investigation of groundwater contamination of potential toxic elements (PTEs) and associated health risks of southern region of Delhi, India. *Chemosphere*, *378*, 144398.

83. Vďačný, M., Puškelová, Ľ., & Michalík, J. (2025). Comprehensive provenance study of the Triassic-Jurassic boundary interval in the Zliechov Basin (Western Carpathians, Slovakia). Journal of Earth System Science, 134(2), 92.

84. Wang, Z., Wang, Y., Shi, M., Ji, W., Li, R., & Wang, X. (2024a). Coordinated analysis of groundwater spatiotemporal chemical characteristics, water quality, and potential

human health risks with sustainable development in semi-arid regions. *Environmental Geochemistry and Health*.

85. Wang, Z., Guo, H., Adimalla, N., Pei, J., Zhang, Z., & Liu, H. (2024b). Co-occurrence of arsenic and fluoride in groundwater of Guide basin in China: Genesis, mobility and enrichment mechanism. *Environmental Research*.
86. WHO (2011a) Guidelines for drinking-water quality. 38(4):104-108.
87. Williams, J. R. (1975). Sediment routing for agricultural watersheds 1. JAWRA Journal of the American Water Resources Association, 11(5), 965-974.
88. Zhang, Y., Wu, J., & Xu, B. (2018). Human health risk assessment of groundwater nitrogen pollution in Jinghui canal irrigation area of the loess region, northwest China. Environmental Earth Sciences, 77(7), 273.
89. Zhang HT, Xu GQ, Zhan HB, Chen XQ, Liu MC, Wang MH (2020) Identification of hydrogeochemical processes and transport paths of a multi-aquifer system in closed mining regions. J Hydrol 589(2):125344.
90. Zhang, C., Rao, W., Wu, Z., Zheng, F., Li, T., Li, C., ... & Chu, X. (2024). Anthropogenic impacts and quantitative sources of nitrate in a rural-urban canal using a combined PMF, δ15N/δ18O-NO3-, and MixSIAR approach. *Environmental research*, *251*, 118587.
91. Zouhri, L., El Amari, K., Hibti, M., Benkaddour, A., & Zghibi, A. (2025). Geochemical assessment and transfer of potential effects of metallic trace elements around abandoned mining sites in Kettara region (Morocco). *Ore and Energy Resource Geology*, *18*, 100076.

Supplementary Files

This is a list of supplementary files associated with this preprint. Click to download.

- SupplementryMaterial.docx